Toluene and 2-propanol mixture oxidation over Mn2O3 catalysts: Study of inhibition/promotion effects by in-situ DRIFTS

E.J. Moreno-Román, J. González-Cobos, N. Guilhaume, S. Gil

Toluene and 2-propanol mixture oxidation over Mn_2O_3 catalysts: Study of inhibition/promotion effects by *in-situ* DRIFTS

E.J. Moreno-Román, J. González-Cobos, N. Guilhaume, S. Gil*

Univ Lyon, Université Lyon 1, CNRS, UMR 5256, IRCELYON, 2 avenue Albert Einstein, Villeurbanne, F-69622, France.

Corresponding author: *sonia.gil@ircelyon.univ-lyon1.fr

Abstract.

Three Mn_2O_3 catalysts were synthetized by different methods, characterized and tested in toluene and 2-propanol (iPrOH) oxidation in single and binary component mixture. In single VOC media, the catalytic activity was strongly influenced by the specific surface area, low-temperature reducibility and active surface-oxygen species. In the binary VOCs mixture oxidation, light-off curves were shifted to lower temperatures, suggesting a promoting effect on the catalytic activity for toluene and iPrOH oxidation. The acetone production in binary mixture was also shifted to lower temperatures. The obtained results were rationalized based on the different polarity of the VOCs, the available adsorbed oxygen and the exothermic character of the VOCs combustion. These promoting effects were pointed out by *in-situ* DRIFTS measurements, in which the pre-adsorption of any of these two VOCs affected the adsorption/reaction of the other. For the first time, *in-situ* DRIFTS has been applied to elucidate the reaction mechanisms of the oxidation of toluene/2-propanol mixture on Mn_2O_3, which allowed to correlate the surface phenomena and the catalytic performance.

***Keywords*:** Manganese oxides-based catalysts, VOCs binary mixture catalytic oxidation, *in-situ* surface measurements, reaction mechanisms.

1. Introduction.

Nowadays, the indoor air pollution is considered as a major public concern. Volatile organic compounds (VOCs) are one of the most dominant air pollutants and known as the main precursors for particulate matter and ozone formation via photochemical reactions. Due to their toxicity, carcinogenic effect and high chemical stability, VOCs present risks to environment and human health [1, 2]. VOCs are emitted from large variety of sources such as solvent use, organic chemical materials production, textile dyeing and printing, leather manufacturing and adhesive manufacturing, among others [3]. VOCs can be classified into saturated alkanes, unsaturated alkenes, chlorinated VOCs, aromatic hydrocarbons and oxygen-containing VOCs [4]. Among all of them, toluene is commonly used as solvent in the chemical industry and the main contributor to photochemical smog formation [5]. Moreover, 2-propanol (iPrOH) is also widely used as a solvent in different industries such as building materials, petroleum refineries, textile, pesticide formulations, pharmaceutical and body care industries [6]. Therefore, toluene and iPrOH can stem from the same emission sources [4].

Given the environmental impact and toxicity of VOCs, European Union (EU) has been regulating the VOCs emission since 1999 by legislation. According to the Goteborg protocol from 2006, which was amended in 2012, EU countries barely met their 2020 reduction commitments for these pollutants (28% reduction, on average, versus 2005) and a further decrease up to 38% has been projected for 2030 [4,7,8]. In the recent years, several non-destructive techniques have been widely applied for VOCs emissions control such as absorption, VOC-condensation and membrane separation [9–12]. However, they present practical limitations, e.g. high initial capital investment, non-easy design, used of solvents, high concentration requirements, extreme-operating conditions (temperature and pressure) and high operating costs, *etc*. On the other hand, destructive technologies for VOCs combustion have been applied such as thermal incineration and catalytic oxidation, which are the most common routes for VOCs mineralization, in medium and high concentrations, into CO_2 and H_2O [3]. Thermal incineration operates at high temperatures around 800-1200 °C for full VOCs degradation, while the catalytic oxidation could convert the VOCs at temperatures of ca. 200-500 °C without the formation of dioxins or other toxic products. Thus, the catalytic oxidation is considered as a promising VOCs removal technology [11,12].

Due to outstanding advantages of VOCs catalytic oxidation, numerous efforts have been put into the development of effective catalysts, where metal oxides or

supported metals have been extensively applied as promising candidates [15]. Noble-metal catalysts such as Pt, Pd, Au, Ag, Rh [15–17] are well known for exhibiting high activities for VOCs abatement and have been applied in some industrial processes such as treatment of motor vehicle exhaust. However, these metals are penalized for their high cost, low thermal stability and susceptibility to poisoning [14]. Non-noble metal oxides catalysts such as CuO, FeO_x, CoO_x, CrO_x and MnO_x oxides have been investigated, showing promising catalytic properties compared to noble-metal catalysts due to their high catalytic performance for diverse VOCs total oxidation and their lower production cost [18–22]. Among the metal oxide-based catalysts, MnO_x oxides have attracted much research attention due to its notable performance in single VOCs removal, easy and low-cost preparation methods [14]. It is well known that the preparation method has an important influence in VOCs oxidation. Sihaib et al. [23] and Zhang et al. [24] prepared MnO_x materials by using different routes. These materials were then used as catalysts for toluene total oxidation. They showed that the specific surface area as well as the reducibility were the main properties that could enhance the oxidation of toluene. On the other hand, Ye et al. [25] also demonstrated that the oxygen mobility, the specific surface area and the redox properties could be tuned by using different preparation methods.

Moreover, the industrial emissions usually contain a mixture of different kinds of VOCs. However, not many studies have been focused on catalytic oxidation of VOCs mixture [17,26–35]. Some of these authors showed an inhibition or promoting effect when the catalytic oxidation of a mixture of VOCs was compared to single VOC oxidation [17,26–35]. For example, Papaefthimiou et al. [33] studied the binary mixture of benzene and ethyl acetate over Pt-based supported catalysts, in which the benzene oxidation seemed to be strongly inhibited by the presence of ethyl acetate. Ordóñez et al. [34] and Wang et al. [26] have also studied binary mixtures over Pt supported catalysts on γ-Al_2O_3 and TiO_2 catalysts, repetitively, where toluene competes with other VOC (either benzene or acetone) for the same active sites. The total oxidation of acetone for example is strongly affected by the presence of toluene since the adsorption capacities of both toluene and acetone are affected [26]. Concerning the acetone-toluene mixture, contrary to the previous study, mutual promoting effect was observed by Blasin-Aubé et al. [27] over $La_{0.8}Sr_{0.2}MnO_{3+x}$ perovskite catalysts. Both acetone and, notably, toluene conversions were shifted to lower temperatures in the binary mixture. A competition for the same adsorption sites was also observed by Aguero et al. [32] over MnO_x/Al_2O_3

catalysts during the simultaneous oxidation of ethyl acetate and ethanol. The inhibiting effect on ethanol oxidation was attributed to the polar character of both molecules. Nevertheless, the presence of toluene had a promoting effect on both ethyl acetate and ethanol partial oxidation, enhancing acetaldehyde yield but decreasing CO_2 one. Musialik-Piotrowska et al. [35] also pointed out an increase of yielded by-products, *i.e.* products from incomplete oxidation, in detriment to the oxy-derivatives oxidation, over $LaMn_2O_3$ perovskite catalysts. The competitive adsorption, in which VOCs compounds inhibit each other, was also observed by He et al. [28] with a benzene-toluene binary reaction mixture over Pd/ZSM-5 catalyst. Interestingly, the presence of ethyl acetate, which has an inhibitory effect on benzene oxidation, promotes the conversion of toluene when both VOCs are in the same reaction mixture. A promoting effect was recently observed by Pan et al. [31] over manganese-based catalysts. These authors showed that the presence of acetone and/or ethyl acetate in the reaction media promotes the formation of new toluene intermediates, which enhanced its conversion at low temperature. A promoting effect at high temperature was also observed, which was attributed to the exothermic character generated by the oxidation of the other VOCs presented in the mixture. Regarding iPrOH-containing mixtures, Burgos et al. [29] showed that the complete oxidation of toluene and methyl ethyl ketone (MEK) is not strongly affected by the presence of iPrOH over $Pt/Al_2O_3/Al$ monoliths. However, the presence of toluene can have an inhibitory effect on the conversion of iPrOH to acetone. Moreover, acetone is prone to be further oxidized to CO_2 and H_2O at lower temperatures in the presence of VOCs mixture. The latter effect was attributed to the previously mentioned exothermic character, which increases the local temperature on the catalyst surface. Beauchet et al. [30] proved that iPrOH combustion was also strongly inhibited by the addition of o-xylene into the oxidation reaction mixture over NaX zeolites. Moreover, the competitive adsorption of o-xylene also influenced the formation of some by-products such as propene and acetone. Thus, apart from the inhibiting or promoting effects on the catalytic activity, the selectivity and the formation of intermediates species can also be affected when VOCs are oxidized in binary mixtures. Nevertheless, the promoting/inhibiting effects depend on the catalyst used, the affinity of VOCs with the catalyst surface and the composition of the VOCs mixture, making it very difficult to predict the behavior of each compound in the mixture or the mechanism involved in such reaction [27,31].

Therefore, the main goal of this work is to understand the effect of the mixture of VOCs in their deep oxidation over three Mn_2O_3 catalysts synthetized by different preparation methods (Citrate-Gel, Pluronic P_{123} surfactant and Glycerol decomposition) [29–31]. These catalysts have been characterized by several techniques and tested for toluene and iPrOH total oxidation both in single reactant and binary mixture oxidation reaction media. This is, to our knowledge, the first time that the catalytic performances (activity and selectivity) of Mn_2O_3 catalysts are evaluated under toluene and iPrOH binary mixture, which will allow to evaluate the promotion/inhibit effects of the competitive adsorption of these VOCs compounds. Moreover, the surface catalytic behavior under VOCs mixture was evaluated by *in-situ* Diffuse Reflectance Infrared Fourier Transform Spectroscopy (DRIFTS), which will allow to spotlight the changes on intermediates species formation in comparison to single VOCs oxidation and elucidate a reaction mechanism for both toluene and iPrOH oxidation.

2. Experimental.

2.1. Synthesis of catalysts.

Different synthesis routes were selected for the preparation of Mn_2O_3 catalysts.

a) Mn_2O_3 catalyst preparation by using Citrate-Gel method (CG-1).

A Citrate-Gel synthesis method was used to prepare Mn_2O_3 catalysts which can be found in a previous study [36]. An aqueous solution was prepared with $Mn(NO_3)_2 \cdot 6H_2O$ and mixed with citric acid in the proportion of one mole citric acid per mole of nitrate. The pH of the solution was adjusted at 6-7 by addition of concentrated ammonia. This solution was heated at 90 °C under stirring (400 rpm), until a viscous gel was formed. Then, the gel was dried at 120 °C in an oven for 15 h. Finally, the powder was grinded in a mortar and calcined at 500 °C for 4 h in air by using a heating ramp of 2 °C min^{-1}.

b) Synthesis of Mn_2O_3 catalyst by triblock copolymer poly(ethylene glycol)-poly(propylene glycol)-poly(ethylene glycol) surfactant (named Pluronic P_{123}) method (P_{123}-1).

Manganese oxides catalysts have been prepared by using P123 surfactant and the details can be found in the previous literature report [37]. A solution was prepared in the desired stoichiometric ratio with 2-butanol, HNO_3 and P123 surfactant in a 150 mL

beaker at room temperature and under magnetic stirring (600 rpm). Then $Mn(NO_3)_2 \cdot 6H_2O$ was dissolved in the solution aforementioned. The obtained pink gel was heated at 120 °C for 8 h. The obtained powder was centrifuged and washed several times with ethanol and water, and then the sample was dried at 100 °C overnight. The dried powder was subjected to three consecutive heating cycles (150 °C for 12 h + 250 °C for 6 h + 350 °C for 4 h) and between each cycle the sample was cooled at room temperature. Finally, the obtained powder was calcined at 500 °C for 4 h in air with a heating ramp of 2 °C min^{-1}.

c) Synthesis of Mn_2O_3 catalyst by Glycerol precipitation method (GM-1).

Two solutions at 0.5 M were prepared: solution "A" was prepared by adding the desired volume of glycerol and $Mn(CH_3COO)_2 \cdot 4H_2O$ and a solution "B" was prepared by adding the desired volume of glycerol and $(NH_4)_2CO_3$. Both solutions were mixed to formed a solution "C", which was stirred and heated at 50 °C until a brown solution was completely formed. Finally, the resultant solution was evaporated/calcined at 500 °C in air for 4 h with a heating ramp of 2 °C min^{-1} to obtain the final catalyst powder.

2.2. Catalysts characterization

The chemical composition, presence of crystalline phases and their identification were evaluated by X-ray diffraction analysis (XRD) using a Bruker D8 Advanced A25 diffractometer, equipped with radiation Cu $K\alpha_{1+2}$ (λ=1.5Å) and detector LynxEye with 2θ from 4° to 80° and using a step of 0.02°. The average of the crystalline size of the catalysts was calculated using Scherrer equation.

High-resolution transmission electron microscopy (TEM) was performed in a JEOL 2010 LaB6 instrument with 200 kV acceleration voltage.

The catalysts textural properties were analyzed by nitrogen adsorption at 77 K using a Belsorp II adsorption measurements apparatus. Previous to adsorption, the catalysts (ca. 300 mg) were degassed at 300 °C under vacuum overnight. The specific surface area and pore size distribution were calculated from the Brunauer-Emmett-Teller (BET) equation and Barret-Joyner-Halenda (BJH) method calculated from the desorption isotherm, respectively.

H_2 temperature programmed reduction (H_2-TPR) and O_2 temperature programmed desorption (O_2-TPD) experiments were performed on a TPDRO 1100 equipment (Thermo Scientific) equipped with a thermal conductivity detector (TCD). For

the H_2-TPR tests, first, the catalysts (50 mg) were pretreated at 500 °C (10 °C min^{-1}) for 1 h with 40 mL min^{-1} of 5% O_2/He and then cooled down to room temperature (RT) under the same stream. After an Ar purge, the H_2-TPR was carried out by introducing 30 mL min^{-1} of 5% H_2/Ar and heating from 30 °C to 900 °C (10 °C min^{-1}). The H_2 consumption was quantified by integration of H_2-TPR profiles. For the O_2-TPD tests, the sample (50 mg) was first pretreated with He (30 mL min^{-1}) at 80 ºC for 1 h, then cooled to 30 ºC and exposed to 5% O_2/He stream (30 mL min^{-1}) for 1 h. Finally, the temperature was increased from 30 to 800 ºC (10 ºC min^{-1}) under He stream (30 mL min^{-1}).

X-ray photoelectron spectroscopy (XPS) was used to analyze the relative content and chemical states of surface elements. The measurements were performed on a Kratos Axis Ultra DLD with an X-rays source Al monochromatic (1486.6 eV), 12kV x 15mA. All the spectra were recorded from 1200 to 0 eV with an energy pass of 160 eV. High resolution spectra were recorded for the Mn $2p_{3/2}$, Mn $2p_{½}$, O 1s, C 1s and Mn 3s with an energy pass of 40 eV. The charge neutralization was done with a low energy electron beam. The spectra are calibrated in binding energy by using C 1s (C-C, C-H) photoemission peak at 284.8 eV.

Raman spectroscopy was also used using a LabRam HR Evolution Horiba spectrometer in the range from 100-1000 cm^{-1} with an excitation light of 532 nm and resolution of 4 cm^{-1}.

Temperature-Programmed ammonia Desorption (NH_3-TPD) was used to assess the acidic properties of the catalysts. Samples were loaded into a U-shaped quartz tube to acquire the NH_3-TPD profiles. All samples were initially pre-treated at 500 °C for 0.5 h in an oxidative environment (10% O_2, 20 mL min^{-1}, heating rate of 10 ºC min^{-1}). After 0.5 h, a He stream (20 mL min^{-1}) was introduced, and the temperature was decreased to 80 ºC, where NH_3 adsorption occurred (a total flow of 40 mL min^{-1} of 1000 ppm NH_3 was introduced until saturation). After that, the samples were exposed to He for 0.5 h to eliminate the physically adsorbed species. Then, NH_3-desorption experiments were performed by heating (at 10 °C min^{-1}) from 80 to 400 ºC. A NICOLET Fourier Transform Infrared (FTIR) analyzer, equipped with a heated 2 m gas cell and a DTGS detector, was used to continually monitor desorbed ammonia.

2.3. VOCs catalytic oxidation.

The catalytic performances were evaluated using a Pyrex fixed-bed U-shape micro-reactor. The catalysts (40 mg of catalyst mass) were sieved in the grain size 200-300 µm and loaded in a catalyst-quartz mixture at a 1:9 wt. ratio. The reactor was placed inside an electric furnace with temperature control and simultaneous recording of the temperature on the furnace wall and inside the reactor with K-type thermocouples. The reactor was fed with a VOC-He stream, produced by injecting liquid VOC (toluene, iPrOH or mixture of both of them) by syringe pump (Harvard Apparatus Elite 11, liquid pump) through an evaporator at 200 °C in order to obtain the desired concentration. Three different reaction atmospheres have been evaluated: i) toluene/air/He (600 ppm of toluene, 20 vol.% O_2), ii) iPrOH/air/He (800 ppm of iPrOH, 20 vol.% O_2) and iii) VOCs mixture (600 ppm of toluene and 800 ppm of iPrOH, 20 vol.% O_2) with a total flow rate of 200 ml min^{-1} and a Gas Hourly Space Velocity of 26450 h^{-1}. These operational conditions allowed to work under kinetic regime. The reactor outlet stream was monitored by a Mass spectrometer and a Micro Gas Chromatograph Inficon 3000 (SRA Instruments) to quantify the concentration of reactants and products. He was used as a carrier gas for both analyzers. Light-off curves were recorded at a heating rate of 2 ± 0.1 ºC min^{-1} and they have been reported after three consecutive catalytic cycles during the cooling ramp.

The overall toluene and iPrOH conversions ($X_{C_7H_8}$ and $X_{C_3H_8O}$, respectivetly) were defined, as a given temperature, as follow:

$$\boldsymbol{X_{C_7H_8}}\ (\%) = \frac{([\boldsymbol{C_7H_{8_{in}}}]) - ([\boldsymbol{C_7H_{8_{out}}}])}{([\boldsymbol{C_7H_{8_{in}}}])}\boldsymbol{x\ 100}\quad \boldsymbol{(1)}$$

$$\boldsymbol{X_{C_3H_8O}}\ (\%) = \frac{([\boldsymbol{C_3H_8O_{in}}]) - ([\boldsymbol{C_3H_8O_{out}}])}{([\boldsymbol{C_3H_8O_{in}}])}\boldsymbol{x\ 100}\quad \boldsymbol{(2)}$$

where the $[C_7H_{8_{in}}]$ and $[C_3H_8O_{in}]$ correspond to the initial inlet concentrations of toluene and iPrOH and $[C_7H_{8_{out}}]$ and $[C_3H_8O_{out}]$ refer to the outlet concentration of toluene and iPrOH.

Moreover, the yield of CO_2 from toluene and iPrOH oxidation as well as the acetone (C_3H_6O) yield form iPrOH oxidation were calculated, at a given temperature, by equations 3 to 5:

$$\boldsymbol{CO_2\ yield}_{\boldsymbol{C_7H_8\ oxidation}}\ (\%) = \frac{([\boldsymbol{CO_{2\ out}}])}{([\boldsymbol{C_7H_{8_{in}}}] * \boldsymbol{7})}\boldsymbol{x\ 100}\quad \boldsymbol{(3)}$$

$$\boldsymbol{CO_2\ yield}_{\boldsymbol{C_3H_8O\ oxidation}}\ (\%) = \frac{([\boldsymbol{CO_{2\ out}}])}{([\boldsymbol{C_3H_8O_{in}}] * \mathbf{3})} \boldsymbol{x}\ \mathbf{100}\ \ (\mathbf{4})$$

$$\boldsymbol{C_3H_6O\ yield}\ (\%) = \frac{([\boldsymbol{C_3H_6O_{out}}])}{([\boldsymbol{C_3H_8O_{in}}])} \boldsymbol{x}\ \mathbf{100}\ \ (\mathbf{5})$$

where the $[CO_{2_{out}}]$ and $[C_3H_6O_{out}]$ refer to the outlet concentrations of CO_2 and acetone.

Furthermore, the overall and specific reaction rates of toluene or iPrOH per mass unit of catalyst or specific surface area were estimated by equations 6 and 7, respectively:

$$-\boldsymbol{r}_{\mathrm{VOC}}(\ \mu\mathrm{mol\ s^{-1}g_{cat}^{-1}}\ ) = F_{\mathrm{VOC}}^{\mathrm{in}} \times \frac{X_{\mathrm{VOC}}}{m_{\mathrm{cat}}}\ (6)$$

$$-\boldsymbol{r}_{\mathrm{VOC,specific}}\ (\ \mu\mathrm{mol\ s^{-1}}\ m^{-2}) = F_{\mathrm{VOC}}^{\mathrm{in}} \times \frac{X_{\mathrm{VOC}}}{m_{\mathrm{cat}} \times S_{\mathrm{BET}}}\ (7)$$

where $F_{\mathrm{VOC}}^{\mathrm{in}}$ is the toluene or 2-propanol molar flow in the inlet, X_{VOC} is the toluene or 2-propanol conversion at 290 and 120 °C, respectively, m_{cat} is the catalyst mass (g) and S_{BET} is the specific surface area determined by N_2 adsorption-desorption. The reaction temperatures were selected with the aim of comparing the reaction rates when the VOC conversion (X_{VOC}) is below 20%.

2.4. In-situ diffuse reflectance infrared spectroscopy (DRIFTS) analysis.

In-situ DRIFTS experiments were carried out in a spectrometer Nicolet iS50 FT-IR using a praying mantis accessory (HARRICK high temperature test chamber) and liquid N_2-cooled MTC detector with a resolution of 2 cm^{-1}. The spectra were recorded from 1000 to 4000 cm^{-1}. The background spectrum was recorded on pure and dry KBr.

Prior to toluene adsorption and reactions experiments, the catalyst was pretreated under high-purity He with a flow rate of 40 mL min^{-1} at 150 °C during 90 min in order to remove the adsorbed water and other surface pollutants. Then, background spectra were collected under the same gas stream (high-purity He) at each work temperature (35, 100, 150, 200, 300 and 400 °C) and systematically subtracted from the sample spectra. After that, the adsorption and oxidation measurements were carried out from 35 °C up to 400 °C under the same reaction atmospheres as those described in previous section (*i.e.*, toluene/air/He, iPrOH/air/He and toluene/iPrOH/air/He), as well as in the absence of gaseous oxygen. The spectra were recorded after exposing the catalyst surface to each reaction atmosphere for 30 min, reaching steady-state conditions. Before introducing each

gas atmosphere, a He flush was applied to remove the weakly physisorbed VOC. The reported spectra are the result of subtracting from the spectra measured at each temperature during the adsorption and/or oxidation of VOCs the reference one collected under He flow at the corresponding temperature before any adsorption.

3. Results and Discussion

3.1. Physico-chemical, textural and structural properties.

The powder XRD patterns of Mn_2O_3 catalysts synthetized by the different preparation methods (Citrate-Gel, Pluronic P_{123} surfactant and Glycerol precipitation, labeled as CG-1, P_{123}-1 and GM-1, respectively) are shown in Figure 1. All of them presented the same diffraction peaks, which are indexed to the cubic bixbyite Mn_2O_3 oxides, according with the PDF 04-007-0856 reference, although the minor presence of MnO_2 cannot be fully discarded. This indicates that the preparation method did not have an important influence on the main manganese oxides phase formation. The main reflections were located at $2\theta = 23.3°$, 32.9°, 38.1°, 45.1°, 49.4°, 55.2° and 65.7° without evidences of any other manganese oxide phase or any impurities. In addition, the crystallite size of the catalysts was calculated by Scherrer equation (Table 1), CG-1 and GM-1 catalysts presenting smaller crystallite sizes than P_{123}-1 catalyst. On the other hand, TEM images (Figure S1 in Supplementary Information) show that the three synthetized catalysts were composed of big MnO_x agglomerates and grains with a heterogeneous shape and size (between 10 and 50 nm in all cases).

The textural properties of the prepared catalysts were characterized by N_2 adsorption-desorption. The sorption isotherms and pore size distributions are shown in Figure S2, and the specific surface area, total pore volume and average pore size are summarized in Table 1. All the catalysts displayed a type-IV adsorption-desorption isotherms at relative high pressure ($0.7 \leq P/P_0 \leq 1.0$), which are characteristic of mesoporous materials, as also reported for other Mn_2O_3 catalysts [39]. The specific surface area (S_{BET}) of CG-1 (24 $m^2\ g^{-1}$) was larger than that of GM-1 (19 $m^2\ g^{-1}$) and even more than that obtained for P_{123}-1 (9 $m^2\ g^{-1}$) catalyst. Moreover, although similar pore size distributions were observed for all catalysts, the total pore volume is influenced by the preparation method used. Thus, the catalysts CG-1 and GM-1 showed a larger pore volume (0.11 $cm^3\ g^{-1}$) in comparison with P_{123}-1 catalyst (0.06 $cm^3\ g^{-1}$). These results

indicate that the preparation method did have an impact on the textural properties of the catalysts.

3.2. Surface and redox properties.

Figure 2a shows the H_2-TPR profiles of Mn_2O_3 catalysts prepared in the present work. Two main reduction peaks are clearly observed. The low temperature reduction peak was attributed to the reduction of Mn_2O_3 to Mn_3O_4, while the high temperature reduction peak was assigned to the reduction of Mn_3O_4 to MnO [23,39–42]. Even though all the catalysts presented similar reduction profiles, the reduction temperatures were different: 354 °C and 486 °C for GM-1, 360 °C and 496 °C for CG-1; 457 °C and 544 °C for P_{123}-1. Thus, the temperature reduction peaks were shifted to higher temperature in the following order: GM-1 < CG-1 < P_{123}, although they were very similar in the two former cases. Moreover, a higher initial hydrogen consumption rate (evaluated on the first peak at low temperature) has been typically associated with a higher reducibility of the catalyst by some authors [43,44]. In this sense, CG-1 catalyst showed the highest initial H_2 consumption rate according to the steepest first reduction peak. This indicates that the CG-1 catalyst presented the highest reducibility among the Mn_2O_3 catalysts used in this work. Note that a first small reduction peak was observed in the H_2-TPR profile of P_{123}-1 catalyst (343 °C), which could be attributed to the surface reducible oxygen species according to the literature [45]. On the other hand, some hydrogen consumption due to the reduction of minor MnO_2 phase could not be discarded to occur at this low temperature peak, as well as its overlapping in the first peak observed for the other catalysts [46–48]. Furthermore, the overall H_2-consumption of the Mn_2O_3 catalysts was calculated from the H_2-TPR profiles and the results are presented in Table 2. Comparing the H_2-consumption per mass of sample obtained for each catalyst as a function of the preparation method, the CG-1 catalyst showed the highest amount (9.1 $mmol_{H2}$ g^{-1}) compared to that obtained for GM-1 (5.7 $mmol_{H2}$ g^{-1}) and P_{123}-1 (6.3 $mmol_{H2}$ g^{-1}) catalysts, which is an indication of the superior oxygen mobility in the MnO_x lattice in the former case, as it has been verified below by O_2-TPD.

Figure 2b shows the O_2-TPD profile obtained with samples of the three as-synthesized catalysts, which allows to obtain insights on the type and relative quantity of oxygen species on the catalysts. Different desorption regions could be highlighted. As it is widely accepted in the preceding literature [39,45,48–54], physically adsorbed oxygen is the most easily desorbed oxygen species, at temperatures below 200 ºC, while

subsequent oxygen desorption up to 400 ºC is typically attributed to chemically adsorbed oxygen. The oxygen desorbed at temperatures of 400-600 ºC is attributed to lattice O^{2-} in the vicinity of the surface and that desorbed at temperatures higher than 600 ºC is related to bulk lattice O^{2-}, which may diffuse to the surface through vacancies generated upon desorption of the surface lattice oxygen. In the present study, CG-1 catalyst showed the highest desorption at temperatures below 200 ºC, *i.e.*, related to physisorbed O_2, denoting a higher amount of active sites with respect to GM-1 and P_{123}-1 catalysts. At higher temperatures, the desorbed oxygen at 200-300 ºC and 300-400 ºC could be tentatively assigned to chemisorbed O_2^- and O^- surface species, respectively [48,52]. Thus, the capacity to adsorb oxygen species, which is strongly affected by the amount of surface vacancies, decreased in the following order: CG-1 > GM-1 > P_{123}-1. Regarding the oxygen desorption observed at 400-600 ºC, it could be attributed to near-surface lattice oxygen, although it is assigned by some authors to bulk lattice oxygen in MnO_2 upon its reduction to Mn_2O_3 [50,54]. This desorption peak was significantly lower in CG-1 catalyst, but its relatively lower desorption temperature denotes a likely better lattice oxygen mobility, which would decrease in the following order: CG-1 > GM-1 > P_{123}-1. Finally, the oxygen evolution observed when the temperature rises above 600 ºC could be assigned to lattice oxygen in bulk Mn_2O_3, while it is subsequently transformed to Mn_3O_4.

These results confirm that the preparation method also had an important influence on the redox properties. The Citrate-Gel method benefited the formation of a catalyst (CG-1) with a higher degree of reducibility. According to Mars-Van Krevelen (MVK) mechanism and previous studies [28,45,51,55–58], these properties facilitate the catalytic oxidation of VOCs because this catalytic reaction occurs when the VOCs interact with the catalyst surface oxygen (chemisorbed or lattice oxygen), giving rise to a reduction/oxidation redox cycle, *i.e.*, reduction of oxide catalyst and its re-oxidation by oxygen from the gas phase. This indicates that GM-1 and CG-1 catalysts are expected to have a better catalytic activity, as will be proven in the next section.

In addition, the XPS analysis were carried out to evaluate the surface oxidation state and surface composition of the synthetized Mn_2O_3 catalysts. Figure 3 shows XPS spectra of the different catalysts, while the surface composition is summarized in Table 2. In particular, Figure 3a shows the XPS spectra in the region of Mn 3*s*. According to

Liu et al. [2], the ΔEs in the splitting of the Mn 3*s* peaks for MnO_2, Mn_2O_3 and MnO is 4.7, 5.5 and 6.0 eV, respectively, which allows to elucidate the oxidation state of catalysts. Indeed, all the spectra showed a similar ΔEs of 5.04 for CG-1 and P_{123}-1 catalysts and 5.07 for GM-1, indicating that Mn^{3+} was mainly presented on all the catalysts. In this sense, the average oxidation state (AOS) of synthetized Mn_2O_3 catalysts, which was determined by the ΔEs of Mn 3s patterns based on the following formula: AOS = 8.956-1.126 * ΔEs (eV) [49,50,59], was 3.28 and 3.25, respectively, confirming that the fraction of Mn^{3+} was the highest. These results are in well agreement with XRD patterns (Figure 1), in which a cubic bixbyite Mn_2O_3 oxides phase was mainly observed. Raman spectra (Figure S3) also confirm this assumption for all catalysts. Indeed, Raman active modes at 312, 454–571, 622-645, 700 cm^{-1} were clearly observed, which are attributed to the out-of-plane bending modes, the asymmetric stretching of bridge oxygen species (Mn-O-Mn) and symmetric stretching of Mn_2O_3 [60–63]. Additionally, GM-1 and P_{123}-1 catalysts presented a highly intense band at 651 cm^{-1}, which can be also attributed to Mn_3O_4 phase [64]. It is worth to mention that the Mn^{3+} species have been related to the oxygen vacancy sites by several authors [50,59,65,66], which have an important role on VOCs oxidation. Indeed, the catalyst oxygen vacancies act as adsorption and activation sites for gaseous oxygen, generating active oxygen species, which easily react with adsorbed VOCs during the oxidation via MvK mechanism [50,59].

On the other hand, the Figure 3b shows the Mn $2p_{1/2}$ and $2p_{3/2}$ spectra for CG-1, P_{123}-1 and GM-1 catalysts. The Mn $2p_{3/2}$ spectrum was deconvoluted into two peaks at binding energy of 641.13 and 642.8 eV, respectively, which are ascribed to Mn^{3+} and Mn^{4+} species [49,51]. The Mn^{3+}/Mn^{4+} molar ratios were determined and are summarized in Table 2. These results indicate that Mn^{4+} species were also present on the surface of all the catalysts, according to Raman spectra (Figure S3). The Mn^{3+}/Mn^{4+} molar ratios decreased as follows: CG-1 > GM-1 > P_{123}-1, which implies the highest concentration of oxygen vacancies in the former [49,50]. These vacancies are considered as active center sites or oxygen adsorption sites for the catalytic oxidation reaction [50]. Moreover, the ratio between the bands at 581 and 622 cm^{-1}, which could be tentatively assigned to the stretching vibration of Mn-O along the basal plane and the direction perpendicular of MnO_6 groups [67–69], can also indicate that the GM-1 and P_{123}-1 catalysts presented less surface defects. Indeed, the band at 581 cm^{-1} was particularly weak in CG-1 spectrum, which suggests that this catalyst presented the most abundant defects on the surface [69]

and, as a consequence, the highest amount of oxygen vacancies since catalyst defects promotes its formation [67–69].

Moreover, as shown in Figure 3c, the O 1s spectra exhibited two peaks centered at 529.2-529.9 and 531.2-531.5 eV, corresponding to lattice oxygen (O_{latt}) and oxygen adsorbed or chemisorbed oxygen (O_{ads}), respectively [40,51]. As presented in Table 2, the O_{ads}/O_{latt} ratios of CG-1, GM-1 and P_{123}-1 were 0.39, 0.32 and 0.29, respectively. The surface adsorbed oxygen concentration decreased as follows: CG-1 > GM-1 > P_{123}-1, which is in agreement with the trends observed by O_2-TPD and also follows the same trend as the catalyst reducibility [45]. Thus, it can be assumed that the highest amount of adsorbed oxygen species was presented on the surface of CG-1 and GM-1 catalysts, suggesting a higher amount of oxygen vacancies because the gaseous oxygen is usually adsorbed at the catalyst oxygen vacancies [44,49]. The latter assumption is also consistent with the highest proportion of Mn^{3+}. In addition, it is worth mentioning that the higher proportion of oxygen adsorbed species, which are the active oxygen species notably at low temperature [45,47,70], will favor an easier interaction with VOCs, promoting the redox cycle and, as a consequence, the catalytic activity. Thus, these results suggest that the CG-1 and GM-1 catalysts, which present the highest amount of adsorbed oxygen species (and oxygen vacancies), will lead to an easier activation at low temperature, improving catalyst low-temperature reducibility. Besides, the CG-1 catalyst presented the largest specific surface area and, hence, might exhibit more active oxygen species, as similarly obtained by Zhang et al. [45].

3.3. Catalytic performance.

After investigating the structural, textural, redox and surface properties of the synthetized Mn_2O_3 catalysts, their catalytic performances for single toluene or iPrOH as well as binary mixture of both VOCs catalytic oxidation were evaluated.

3.3.1. Single toluene catalytic oxidation.

Figure 4 shows the catalytic activity of Mn_2O_3 catalysts in toluene oxidation reaction in terms of a) toluene conversion and b) CO_2 yield. In particular, Figure 4a shows the light-off curves. No other final by-products (such as CO) were detected besides CO_2 and H_2O, which were likely produced by reaction (8).

$$C_7H_8 + 9\ O_2 \rightarrow 7\ CO_2 + 4\ H_2O;\ \Delta H_{298} = -3771.9\ kJ\ mol^{-1} \quad (8)$$

As listed in Table 3, the temperatures at 90% (T_{90}) of toluene conversion were ranked as follows: CG-1 (337 °C) < GM-1 (348 °C) < P_{123}-1 (373 °C). Firstly, it worthwhile to note that the catalyst with the lowest specific surface area, P_{123}-1 catalyst (9 m^2 g^{-1}, Table 1) presented a lower catalytic activity than those with notably higher specific surface area (24 and 19 m^2 g^{-1} for CG-1 and GM-1, respectively, Table 1). Moreover, the reaction rate and the specific reaction rate at 290 °C of synthetized Mn_2O_3 catalysts are also listed in Table 3, showing that P_{123}-1 has the lowest overall reaction rate (in µmol g^{-1} s^{-1}) but the highest specific reaction rate (in µmol m^{-2} s^{-1}) among the three catalysts. These results suggest that the specific surface area played an important role in the catalytic oxidation of toluene over the synthesized Mn_2O_3 catalysts in this study, which is in agreement with the literature [50,51,71,72]. Nevertheless, the specific surface area is not the only factor determining the toluene oxidation. Thus, the enhanced catalytic performances observed for CG-1 and GM-1 catalysts can be attributed to the larger surface areas but also likely to the higher amount of adsorbed active oxygen (Figure 2b and O_{ads}/O_{latt} ratio in Table 2) and higher low-temperature reducibility (Figure 2a) compared to those of P_{123}-1 catalyst, as also reported elsewhere [45,47,51,58,70,72–74].

3.3.2. Single 2-propanol *(iPrOH) catalytic oxidation.*

iPrOH catalytic activity (iPrOH conversion and acetone and CO_2 yields *vs.* reaction temperature) is presented in Figure 5a-c. Note that for all the catalysts, the acetone is firstly formed, and the only one product obtained at low temperature, notably as a by-product from the dehydrogenation of iPrOH (reaction 9), according to the literature [75,76], and it is then converted into CO_2 and H_2O at increasing reaction temperatures, thus leading to the overall 2-propanol combustion reaction (reaction 10).

$$C_3H_8O \rightarrow C_3H_6O_2 + H_2;\ \Delta H_{298} = +54.1\ kJ\ mol^{-1} \quad (9)$$

$$C_3H_8O + 9/2\ O_2 \rightarrow 3\ CO_2 + 4\ H_2O;\ \Delta H_{298} = -1872.2\ kJ\ mol^{-1} \quad (10)$$

It would be worth mentioning that dehydrogenation of iPrOH takes place through hydride abstraction and is related to the Lewis acidity of oxide catalysts. Mn oxides and notably Mn_2O_3 exhibit Lewis acidity [77]. No others than acetone and CO_2 gaseous by-products were observed. Figure 5a shows the light-off curves, in the range of 50-400 °C, for single iPrOH catalytic oxidation. CG-1 and GM-1 catalysts presented the highest iPrOH conversion at almost all temperature range (*vs.* P_{123}), which can be attributed to the higher amount of low-temperature active oxygen species and low-temperature

reducibility (Table 2, Figure 2) as well as to the higher specific surface area (Table 1) of these catalysts. This indicates that the specific surface area also had an important influence on iPrOH oxidation reaction, as confirmed by the overall and specific reaction rate, Table 4 [75,76,78,79]. Moreover, GM-1 catalyst presented the highest iPrOH conversion at very low temperature (T_{25}, Table 4), while a higher and similar activity was observed for CG-1 catalyst at intermediate and high temperatures, respectively (T_{50} and T_{90}, Table 4). This activity dependence on the reaction temperature could be associated to the differences on reduction profiles between both catalysts (Table 2), but also to the higher moderate acidity of the latter (75 μmol g^{-1} of total amount of NH_3 desorbed for CG-1 *vs.* 44 μmol g^{-1} for GM-1, according to NH_3-TPD measurements, Figure S4). Thus, among all the catalysts, CG-1 presented the highest catalytic activity and selectivity for acetone formation at temperatures above 140 ºC (Figure 5b), which seems to be favored by the catalyst acidity [75,76], while CO_2 yield is relatively higher on GM-1 catalyst (Figure 5c).

3.3.3. Binary VOCs mixture oxidation reaction.

The catalytic activity corresponding to the binary mixture oxidation of toluene and iPrOH VOCs over the synthetized Mn_2O_3 catalysts is depicted in Figure 6 and summarized in Table 5. Interestingly, the tendency on catalytic activity for the different Mn_2O_3 catalysts during the catalytic oxidation of a mixture of VOCs was slightly different than that observed on single VOCs oxidation. Indeed, CG-1 catalyst clearly presented the highest catalytic activity in almost all the temperatures range for toluene and iPrOH during its binary mixture oxidation. These results also showed that the catalytic activity for oxidation of a VOC in a mixture differs from its single oxidation, since the conversions of toluene and iPrOH were shifted to lower temperatures in the binary mixture, Figure 6a and b. This shift suggests that the presence of both VOCs together in a binary mixture had a promoting effect over their catalytic oxidation at the VOCs concentration studied in this work.

Moreover, when the effect of toluene on the iPrOH conversion is checked, Figure 6c shows that the increase of acetone yield is also shifted to lower temperatures than in single iPrOH conditions. This can indicate that toluene did not inhibit the selective conversion of iPrOH to acetone as opposed to some previous works [29]. It worthwhile to note that toluene is one of the VOCs that inhibit in the highest extension the oxidation of the other VOCs notably over Pt-zeolites and alumina-based catalysts, whereas it is

inhibited in a low extension by the other compounds [28,29,34]. Nevertheless, as pointed out by Aguero et al. [32] and Musialik-Piotrowska et al. [35], the toluene can also have a promoting effect on partial oxidation of others VOCs such as ethyl acetate or ethanol over manganese-based catalysts (MnO_x/Al_2O_3 and $LaMn_2O_3$-type perovskite), increasing the yield of by-products derived from their incomplete oxidation, in detriment of the oxy-derivatives oxidation. All these studies indicate that the toluene inhibition/promoting effects depend on the catalyst used. In the present study, a promoting effect on acetone formation was clearly observed since the acetone, derived from the 2-propanol partial oxidation, was formed at lower temperatures in presence of toluene. On the contrary, the CO_2 yield was slightly shifted to higher temperature (Figure 6d), in the almost entire temperature range, comparing to that observed in single iPrOH oxidation (Figure 5c) [26,32,35]. To properly appreciate this effect, the CO_2 yield in mixture and that observed during the single oxidation of toluene and iPrOH over CG-1 catalyst are presented in Figure S5. These results suggest that the presence of toluene in the reaction media favored the iPrOH partial oxidation instead of its total oxidation, which can be attributed to the competitive adsorption of toluene and gaseous oxygen [80]. Thus, some adsorption sites will be occupied by the toluene, decreasing the available oxygen from the gas phase for iPrOH total oxidation. The relationship between the decrease of reactive oxygen and the increase of the selective (partial) oxidation of 2-propanol and other alcohols has been reported in previous works [81,82]. Moreover, Figure 6c shows that acetone in the binary mixture was completely oxidized at lower temperatures than in single oxidation. This latter beneficial effect was attributed by Burgos et al. [29] to the exothermic character induced by the oxidation of others VOCs presented in the mixture, here due to the toluene oxidation. This exothermicity would increase the local temperature on the catalyst surface [29,30], shifting (and enhancing) the complete oxidation of acetone to lower temperatures, Figure 6c. In the same way, the toluene conversion, which starts when almost all iPrOH is oxidized, also shifted to lower temperatures. This indicates that iPrOH, which is the more reactive VOC due to its higher polarity [29,30], initiated the oxidation reaction and the subsequent release of some catalyst active sites for toluene adsorption/transformation, along with the previously mentioned exothermic effect generated by iPrOH/acetone total oxidation. The exothermic effect was systematically evidenced by the slight deviation of the temperature registered inside the reactor, with respect to the heating ramp set at 2 °C min^{-1} at furnace, during the light-off tests for all VOCs oxidation upon reaching a certain temperature (see for example Figure S6). Indeed,

one can observe that the momentary uncontrolled increase in the reactor temperature was noticed at those temperatures at which VOCs combustion reactions (and thus CO_2 evolution) were triggered (c.a. 270 ºC for toluene and 240 ºC for iPrOH and binary mixture on CG-1, Figure S6), which are strongly exothermic (see reactions 8 and 10). Instead, iPrOH dehydrogenation reaction is slightly endothermic (reaction 9). In this way, the iPrOH and acetone total oxidation can promote by a local exothermicity the oxidation of toluene [30–32]. Indeed, Aguero et al. [32] showed that the exothermic effect generated by the oxidation of other VOC presented in the reaction mixture can even compensate the current inhibition of toluene oxidation by the competitive adsorption of CO_2 and H_2O derived from iPrOH mineralization in the present study. Therefore, the exothermicity created by the total oxidation of both VOCs may play a major role in the binary mixture, giving rise to a mutual promotion effect notably at high temperatures. In order to have a better understanding on the promotion or inhibition effects and elucidate the main intermediate species for both oxidations, *in-situ* DRIFTS measurements were carried out and will be presented in the next section.

3.4. Single toluene or iPrOH adsorption and oxidation on CG-1 catalyst assisted by DRIFTS.

In-situ DRIFTS measurements have been performed over the most active Mn_2O_3-based catalyst synthetized in this work, CG-1, under different temperatures and reaction atmospheres. Note that bands attributed to adsorbed CO (1900-2100 cm^{-1}) were not observed in any of the collected spectra (see, for example the full-range spectrum shown in Figure S7). Bands associated to gas CO (2100-2200 cm^{-1}) were neither detected in any case, and those related to gas CO_2 (2300-2400 cm^{-1}) were only detected under certain reaction conditions. All spectra shown herein have been focused on those wavenumber regions where bands associated to the different reaction intermediates have been found.

3.4.1. Single Toluene oxidation: Intermediate by-products generated.

The *in-situ* DRIFTS measurements under air atmosphere were first carried out to investigate the reaction mechanism of toluene oxidation reaction, and the results obtained at different temperatures are shown in Figure 7. The main bands of toluene oxidation intermediates are presented in Table 6.

At 35 ºC, some broad bands were observed at the range of 3060-2872, 1494, 1291 and 1026 cm^{-1}, which are attributed to the C-H stretching vibration of the aromatic ring

in toluene molecule and symmetrical vibration of methyl group [74,83–86]. These bands indicate that toluene molecule was adsorbed on the surface of the Mn_2O_3 catalyst. In addition, some weak bands were identified at 1080 and 1180 cm^{-1}, which are assigned to benzyl alcohol and benzoic acid species (υ(CO-) and υ(C-O) stretching vibrations), respectively [65,87]. The latter suggests that the adsorbed toluene can interact with the catalyst active oxygen species (in particular O_{ads}, XPS results, Table 2), or active surface-adsorbed oxygen species generated via catalyst oxygen vacancies [50,59], to produce benzyl alcohol by breaking the C-H bond of methyl ($-CH_3$) even a low temperature. Moreover, the bands observed at 1405 and 1569 cm^{-1} were assigned to symmetric and asymmetric stretching vibrations (υ_s,υ_a(C=O)) of carboxylate group, respectively, indicating the likely formation of benzoates species [83,88]. A band a 1337 cm^{-1} with a small shoulder at 1300 cm^{-1} was also found, which can be ascribed to maleic anhydrides species, υ(C=O) stretching vibrations [51], hypothetically due to the toluene aromatic ring bond cleavage. The presence of these intermediates' species suggests that the toluene could be partially oxidized at 35 °C on the surface of Mn_2O_3 catalyst. However, these toluene reactions likely took place to a moderate extent at such low temperature, in agreement with the light-off toluene oxidation curves (Figure 4), where temperatures above 250 ºC were required to obtain significant toluene conversion and CO_2 production.

With increasing temperature (100 °C), all the bands associated to surface intermediates, especially those likely attributed to benzoates (υ(C=O) at 1405 and 1569 cm^{-1} [83,88]) and maleic anhydrides species (band at 1337 cm^{-1} and shoulder at 1300 cm^{-1} [89,90]), became more pronounced. Similar behavior was observed by Xu et al. [89]. Moreover, new bands at 1150, 1448 and 1591 cm^{-1} assigned to benzyl alcohol, acetate and benzaldehyde species, respectively, were also observed [83,91]. A similar behavior was observed at 150 °C. Additional weak bands appeared at this temperature, at 1816, 1920 and 1963 cm^{-1}, attributed to maleic anhydrides species [92,93]. Then, at 200 and 300 ºC, several bands clearly decreased like those at 1816-1963 cm^{-1} (maleic anhydride), 1591 cm^{-1} (benzaldehyde), 1448 cm^{-1} (acetate) and 1080-1150 cm^{-1} (benzyl alcohol), indicating the conversion of toluene into CO_2 and H_2O products. This could explain the promotion of acetone oxidation, during the previous-described binary mixture oxidation (Figure 6b). However, toluene was not completely mineralized because some bands of benzoate groups became even more intense at 200 and 300 °C (*e.g.*, 1523 and 1405 cm^{-1}), which could indicate that these species are the main intermediates of toluene oxidation

reaction. These intermediates species still remained even at 400 °C as well as the maleic species, which are represented by a small shoulder at 1300 cm^{-1}. On the other hand, all toluene bands vanished at this high temperature, in agreement with the expected faster toluene desorption with the temperature.

These *in-situ* DRIFTS results of adsorption and oxidation of toluene over CG-1 catalyst can be described by the following reaction pathway:

Toluene → Benzyl alcohol → Benzaldehyde → Benzoic acid → Maleic anhydride → Acetate → CO_2.

A similar reaction pathway was proposed by Xu et al. [89] and Sun et al. [90].

Moreover, the *in-situ* DRIFTS measurements under oxygen-free conditions were also carried out in order to elucidate the catalyst oxygen species participation on toluene oxidation pathway over CG-1 catalyst. The DRIFTS spectra are shown in Figure 8. These results showed again that toluene was adsorbed on the catalyst surface at low temperature (35 °C), which was evidenced by the presence of several bands at 3060-2872, 1600, 1494 and 1291 cm^{-1} related to the aromatic ring symmetric vibrations [83,85]. However, no intermediates bands were detected at 35 °C under oxygen-free conditions, suggesting that the surface-adsorbed oxygen species, coming from gas phase, played an essential role in toluene oxidation at low temperature. As previously mentioned, the catalyst oxygen vacancies accelerate the process of adsorption/activation of gas-phase oxygen, and its absence hinders the reaction of adsorbed toluene to form intermediates by-products [50,59,65]. Moreover, it is important to notice that the bands attributed to the aromatic ring vibrations were less pronounced in this case compared to those obtained in oxygen atmosphere. Some reaction intermediates were nevertheless detected in oxygen-free conditions with the temperature increasing from 100 to 400 °C. At 100 °C, the main intermediate adsorbed species presented were carboxylates (at 1569-1523 cm^{-1} and in the range of 1405-1384 cm^{-1}) [51,83]. From 100 to 300 °C, these intermediate species still remained and increasing bands were, indeed, observed. Additionally, a significant band at 1591 cm^{-1} [74,94], attributed to aldehydes, and weak bands at 1180, 1080 and 1026 cm^{-1} assigned to benzoic acid and benzyl alcohol, were observed at 150 °C and even increased at 200 and 300 ºC. Note that the latter band at 1026 cm^{-1}, that was previously attributed to the toluene ring vibrations [86], can be also assigned to the formation of benzyl alcohol intermediates species [91], which is suggested in this case given the absence of this band

at 35 °C. The weak bands, at 1816, 1920 and 1963 cm^{-1}, previously attributed to maleic anhydrides species were also observed at 200 and 300 °C [92,93], which clearly decreased at 400 °C. These bands were appeared and disappeared at higher temperatures to those observed in oxygen atmosphere, which indicates that these intermediates are difficult to form and mineralize under free-oxygen conditions. These results confirmed that the catalyst surface oxygen (chemisorbed or lattice oxygen) play an important role in toluene oxidation reaction, which is in agreement with the literature [59,90,95]. Finally, the presence of carboxylate and benzaldehyde bands even at 400 °C, without evidenced bands associated to carbon dioxide (not shown), indicates that the aromatic C=C bonds are difficult to cleavage under oxygen-free conditions, in agreement with some literature [65,92]. This leads to a preferred partial oxidation of toluene and so, to the accumulation of some by-products on the surface of the CG-1 catalyst under oxygen-free conditions.

Based on above DRIFTS measurements, it can be concluded that catalyst surface oxygen (chemisorbed or lattice oxygen) could participate in the activation/oxidation of toluene. Nevertheless, the presence of gaseous oxygen and thus the formation of surface adsorbed oxygen species favoured the toluene conversion at lower temperatures (even 35 ºC) and the deep oxidation reactions, in particular. Indeed, no intermediates were clearly observed at low temperature without the replenishment of gaseous oxygen through catalyst oxygen vacancies. Moreover, some key intermediates were difficult to deeply oxidize to H_2O and CO_2 under free-oxygen conditions, which also confirmed this assumption [50,59].

3.4.2. Single iPrOH oxidation: generated surface by-products.

Up to now, the catalytic iPrOH oxidation mechanism is not well known yet, even if it has been studied during the last years [96–98]. In this study, several *in-situ* DRIFTS measurements have been carried out in order to have a better understanding of iPrOH reaction pathway. The main bands of iPrOH intermediates are summarized in Table 7.

As shown in Figure 9, at 35 ºC, the iPrOH was rapidly adsorbed on the surface of CG-1 catalyst. Some adsorption bands were observed in the range of 2969-2872 cm^{-1}, which can be attributed to asymmetric and symmetric methyl (νCH_3) vibrations of iPrOH [96]. The asymmetric methyl bands at 1468 cm^{-1} and the symmetric C-H methyl bands (δ_s CH_3) at 1384 cm^{-1} characteristic of isopropoxide species were also observed, which

denotes a dissociative adsorption of 2-propanol, according to the literature [96–98]. In addition, the two bands at 1164 and 1124 cm^{-1}, as well as a small shoulder at 1215 cm^{-1}, could be attributed to the skeletal δC-C stretch mode vibrations (δ(C-C)) and the methyl (CH_3) rocking vibrations, respectively, which can be all of them also associated to the isopropoxide dissociated species [96,98]. Moreover, the band at 1290 cm^{-1} can be attributed to hydroxyl group of strongly bonded non-dissociated iPrOH species on the CG-1 Lewis acid sites [97]. A band at 1337 cm^{-1} was also observed at low temperature, which can be associated to the acetone [98]. Finally, a band at 1569 cm^{-1} can be related to COO stretching vibrations due formate species formation at 35 °C. This latter band indicates that the acetone could be converted into acetic and formic acids [98] even at low temperature. Indeed, it is worth mentioning that two adsorption ways are described in the literature for iPrOH by using MnO_x as catalysts: i) the dissociative and ii) non-dissociative way [96]. The dissociative adsorption gives rise to the formation of isopropoxy groups and surface hydroxyl species, whereas strongly bonded iPrOH species on catalyst surface Lewis acid sites and weakly hydrogen-bonded iPrOH to surface basic sites are resulting from the non-dissociative adsorption [96,98]. The latter behavior could produce the dehydrogenation of iPrOH to produce acetone [75], which is in agreement to the light-off curves obtained in this study, Figure 5b. Nevertheless, the obtained DRIFTS results suggest that both adsorption modes actually take place on CG-1 catalyst surface.

With the temperature increasing from 35 to 400 °C, the iPrOH oxidation reaction accelerates and some other intermediates were formed. Although band changes were clearly observed, however, the iPrOH still remained on CG-1 catalyst surface. At 100 °C, the iPrOH transformation was evidenced by the decrease of the bands located at 1468 and 1384 cm^{-1} and those in the range 2969-2872 cm^{-1}, 1164-1124 cm^{-1} and 1290 cm^{-1}. On the other hand, the acetone formation was denoted by the two new bands appearing at 1051 and 1419 cm^{-1}, and the increase of the above-mentioned band at 1337 cm^{-1}. These results demonstrated that the iPrOH oxidation to acetone takes place mainly above 100 °C on this catalyst, which is in agreement to catalytic oxidation light-off curves, Figure 5a,b. By increasing the temperature till 150 and 200 °C, less pronounced iPrOH bands were observed (e.g. in the region of 2969 to 2872 cm^{-1}, at 1164 and 1124 cm^{-1}). In addition, the more pronounced bands observed at 1337 and 1437 cm^{-1} suggest the formation of acetone as well as its transformation to the enol form, respectively [98]. Moreover, the band at 1569 cm^{-1}, which can be related to the formation of acetic and formic acids [93], became

more pronounced notably at 200 °C. Finally, all the characteristic vibration bands of iPrOH/acetone oxidation intermediates were clearly decreased at 300 °C and completely disappeared at 400 °C, suggesting the deep oxidation and full conversion of iPrOH, respectively. These results are in agreement with the 100% yield to CO_2 observed in Figure 5c at such high temperatures [92,93]. Thus, the absence of gaseous oxygen is required to observe the continuous increase of produced acetone and other iPrOH-derived intermediates in the 35-400 ºC range. It is also important to note that, as shown for toluene in Figure 7, the iPrOH vibration bands were much less pronounced at temperature above 200 ºC and almost disappeared at 300 °C, which indicates the fast desorption of iPrOH at such high temperatures. Moreover, by comparing the priors DRIFTS spectra obtained during toluene oxidation with those of iPrOH, it is confirmed that CG-1 catalyzed both the formation of intermediates and the full conversion at lower temperatures in the latter case, as previously observed in the light-off measurements.

On the other hand, the Figure 10 presents the spectra of iPrOH adsorption, and its eventually oxidation, over CG-1 catalyst under oxygen-free conditions in order to study the catalyst oxygen species participation on iPrOH catalytic oxidation. As expected, the iPrOH adsorption took place even at low temperature (35 °C), which is indeed represented by the presence of some bands in the range 2969-2872 cm^{-1}, at 1468 and 1384 cm^{-1} [96–98], as well as those previously assigned to δO-H bending, skeletal δC-C stretch mode vibration and methyl (CH_3) rocking vibrations, at 1290, 1164 and 1124 cm^{-1} [96,98]. The bands at 1569 and 1337 cm^{-1}, attributed to formate and acetone, respectively, were also observed denoting a certain iPrOH conversion, even at 35 ºC, due to the participation of catalyst active oxygen species (O_{ads}). By increasing the temperature to 100 °C, the bands associated to iPrOH adsorption became more pronounced, suggesting that iPrOH is accumulated on catalyst surface with a much lower catalytic conversion in the absence of gaseous oxygen (*vs.* Figure 9). Nevertheless, the bands located at 1337, 1419 and 1569 cm^{-1} attributed to the formation of acetone and formate species [75,98], respectively, were clearly observed in the entire range of studied temperatures, increasing in intensity up to 200 °C and even more at 300 °C. The bands related to acetone and formate species were more pronounced than those observed in presence of oxygen (Figure 9 vs. 10) and still remained at higher temperatures (400 ºC). This confirms the iPrOH conversion into acetone and formate even in the absence of gaseous oxygen, *i.e.* by the catalyst lattice

oxygen. However, under these conditions, there was not enough oxygen to produce the total conversion of iPrOH to CO_2, as previously observed in the case of toluene.

Taking account the light-off curves and DRIFTS measurements, both dissociative and non-dissociative adsorption of iPrOH are pointed out, which allows to propose the following mechanism for iPrOH oxidation reaction over CG-1 manganese oxide catalyst:

$$iPrOH \rightarrow Acetone \rightarrow Acetic\ acid \rightarrow Formic\ acid \rightarrow CO_2$$

These results also confirm that both surface-adsorbed oxygen and lattice oxygen on CG-1 catalyst surface participate to the partial oxidation of iPrOH since acetone and formate species are formed under oxygen-free conditions. However, as for toluene oxidation, the adsorbed oxygen should play a major role in iPrOH oxidation, in which the full conversion is not clearly observed without oxygen in the feeding stream. Moreover, these results corroborate that decreasing the oxygen available from the gas phase, the partial oxidation of iPrOH is favored in detriment of the total oxidation. This is consistent with the previous assumptions proposed to explain the shifting at lower temperatures of iPrOH conversion and acetone formation in presence of toluene (Figure 6a and c).

3.4.3. Toluene and iPrOH binary mixture oxidation reaction: promotion/inhibition effects.

In order to investigate the surface mechanism and the inhibition/promotion effects in the presence of both toluene and iPrOH, the spectra were also recorded upon introduction of a mixture of both VOCs and air in the DRIFT cell (600 ppm toluene, 800 ppm 2-propanol, 20 vol.% O_2). Figure 11 shows the DRIFTS spectra for the CG-1 catalyst exposed to a toluene/iPrOH mixture, in which the main bands of iPrOH and some related to the toluene adsorption can be identified. At low temperature, the iPrOH characteristics bands were indeed observed in the region of 2969-2872 cm^{-1} and at 1468 and 1384 cm^{-1} [96]. Also, the bands 1164 and 1124 cm^{-1} associated to the dissociative adsorption of iPrOH were clearly observed [98,99]. However, the main bands of toluene adsorption vibrations such as at 3060, 1494 and 1026 cm^{-1} were not clearly observed in the spectra till 300 °C. Only the band at 2872 cm^{-1} could be eventually identified at 200 °C as the C-H stretching vibration of the aromatic ring in toluene, although this band would be overlapping with the CH_3 vibration of iPrOH molecule. Moreover, the bands in the region of 2969-2872 cm^{-1} and at 1468 cm^{-1} as well as the bands at 1164 and 1124 cm^{-1} related to iPrOH adsorption [96,98,99] disappeared at 300 °C, which could indicate the fast

desorption/transformation of iPrOH at such high temperatures. Nevertheless, the DRIFTS spectrum became at this temperature more similar to that observed for single toluene oxidation (vs. Figure 7 at 300 °C). This suggests that most of the toluene is adsorbed, and oxidized, only after deep or full conversion of iPrOH, probably due to the differences in the polarity of these VOCs. Indeed, it is known that the adsorption of VOCs on manganese-based catalyst surface is governed by its polarity [31,32], giving rise to a competition for the adsorption sites, which clearly affects the transformation of the other, as it is clearly observed in Figure 11. However, at 35 ºC and, specially, at higher temperatures (from 100 to 200 °C), different bands were identified in the range of 1600-1300 cm^{-1} that could be attributed to some of the intermediates derived from either toluene or iPrOH oxidation, according to Table 6 and 7. Given the high overlapping of these bands and the difficult interpretation of these spectra, new measurements were carried out in which toluene and 2-propanol were sequentially introduced as follows: first either iPrOH or toluene was introduced (in air stream) in the DRIFT cell at 35 ºC for 30 min. Then, the weakly physisorbed molecules were swept by He stream for 15 min and the other VOC-air stream was subsequently introduced for 30 min. A DRIFTS spectrum was collected in each VOC atmosphere. In addition, after the introduction of the second VOC, the DRIFT cell was heated to 200 ºC and a spectrum was also collected at this temperature.

Thus, Figure 12 shows the spectra collected at 35 ºC, with the same binary VOCs mixture as in Figure 11, but after performing the 2-steps sequence, where either a first mixture of 600 ppm toluene and 20 vol.% O_2 was first introduced for 30 min (1^{st} step) and it is followed by a He purge and the introduction of a second mixture of 800 ppm 2-propanol and 20 vol.% O_2 (2^{nd} step, leading to the spectrum denoted as "1^{st} toluene"), or the two mentioned mixtures were introduced in the opposite order (spectrum denoted as "1^{st} iPrOH"). For comparison purposes Figure 12 also shows the spectra recorded after 30 min of single toluene or iPrOH adsorption (which represent the first step of the sequential measurements) over the surface of fresh CG-1 catalyst as well as the spectrum obtained after the simultaneous introduction of toluene and iPrOH (denoted as "mixture"). Note that the spectra associated to single toluene or iPrOH were similar to those presented in Figures 7 and 9, respectively, denoting a good reproducibility of the DRIFTS measurements on the Mn_2O_3 catalyst. Therefore, the main bands for toluene and iPrOH adsorption have been described in the previous sections.

When toluene was firstly adsorbed on the fresh CG-1 catalyst surface, the main bands attributed to this molecule were clearly observed (orange profile in Figure 12). However, these bands disappeared after consecutive iPrOH adsorption (brown profile) and were not clearly presented when iPrOH was pre-adsorbed (light blue profile). Nevertheless, the main bands attributed to the adsorption of iPrOH are clearly presented in all cases. In particular, the bands associated to dissociative and non-dissociative adsorption of iPrOH (bands in the range of 2969-2872 cm^{-1} and that at 1468, 1384, 1164 and 1124 cm^{-1} [96,98]) were clearly observed before and after toluene adsorption (dark and light blue profiles in Figure 12). The pre-adsorption of toluene (brown profile) also did not have an important influence on iPrOH adsorption. Nevertheless, in this case, the bands attributed to the formation of formate or acetone intermediates species from partial oxidation of iPrOH (1569 and 1337 cm^{-1} [16,75,98]) were more pronounced, especially the former. This can be related to the previous-mentioned promoting effect induced by competitive adsorption of toluene and oxygen coming from the gas phase, which favors the partial oxidation of iPrOH. It is worth to mention that the formation of some toluene oxidation intermediates such as maleic anhydride and benzoates species, which are currently observed at similar wavelength region, also need to be consider, suggesting that both oxidation reactions take place simultaneously. Thus, these results confirm that the adsorption of iPrOH, which is governed by its higher polarity [29], and its partial oxidation can be preserved and even enhanced by the pre-adsorption of toluene.

On the contrary, by firstly adsorbing iPrOH and then injecting consecutively toluene on iPrOH pre-adsorbed surface of GC-1 catalyst (light blue profile in Figure 12), the main bands attributed to toluene adsorption were almost not observed. Indeed, the bands located in the range 3060-2872, 1494 and 1026 cm^{-1} were not presented. Only a weak band at 1405 cm^{-1} and a weak shoulder at 1569 cm^{-1} assigned to the carboxylate's species formation from toluene oxidation were observed. These results confirm that the adsorption of toluene and the formation of intermediates species were clearly affected by the easy pre-adsorption of iPrOH at low temperature due to its higher polarity [29]. Nevertheless, the presence of some bands related to toluene intermediate species suggests that some catalyst active sites were still available under these conditions. The additional band located at 1692 cm^{-1} (light blue profile in Figure 12), which could be attributed to C=O stretching vibration of the quinone or other ketone species (*e.g.* benzoquinone)

[92,100,101], confirms that the toluene oxidation mechanism and the catalyst selectivity can be also affected by the presence of iPrOH before toluene adsorption.

These *in-situ* DRIFTS measurements at low temperature (35 ºC) suggest that the pre-adsorption of any of these VOCs over a Mn_2O_3-based catalyst affects the adsorption and transformation (*i.e.* intermediates formation) of the other one. At this temperature, the spectrum resulting from toluene introduction after iPrOH pre-adsorption is similar to that obtained after simultaneous VOCs introduction. The pre-adsorption of 2-propanol hinders toluene transformation and change its reaction mechanism with a band associated to ketones species, which is not presented if iPrOH is secondly or simultaneously introduced. On the other hand, the pre-adsorption of toluene promotes the oxidation of iPrOH with an apparent preference for formate *vs.* acetone formation according to the outstanding rise of the band at 1569 cm^{-1} *vs.* 1337 cm^{-1}.

The surface behavior of the Mn_2O_3 catalyst was also investigated after heating the DRIFT cell to 200 ºC in both scenarios, *i.e.* pre-adsorbing toluene or iPrOH (Figure 13). The spectra shown for single toluene, single iPrOH and mixture were the same as those shown at 200 ºC in Figures 7, 9 and 11, respectively. Nevertheless, the formation of intermediates by-products followed a different pathway when the two VOCs were sequentially adsorbed at 35 ºC on the surface of CG-1 catalyst before heating to 200 ºC. Surprisingly, the spectrum recorded under simultaneous adsorption of toluene and iPrOH mixture (red profile in Figure 13) became, at this high temperature, more similar to that corresponding to the subsequently iPrOH adsorption over the pre-toluene adsorbed catalyst surface (brown profile in Figure 13). Nevertheless, the bands associated to the toluene (or iPrOH) intermediates, notably in the range of 1591-1523 cm^{-1}, were more pronounced under simultaneous adsorption of toluene and iPrOH mixture. Taking account that iPrOH has a stronger affinity for Mn_2O_3 surface than the toluene molecule because of its polarity [31,32], these results confirm the promoting effect of 2-propanol pre-adsorption on the toluene transformation at 200 °C. This is in agreement with the shift of toluene conversion to lower temperatures in the light-off curves obtained in binary mixture (Figure 6a), which was induced by the total oxidation of iPrOH (exothermic character, Figure 6b).

This assumption was confirmed by pre-adsorbing iPrOH on surface of CG-1 catalysts (light blue profile in Figure 13). Thus, a different toluene adsorption/reaction

mechanism was observed when iPrOH was previously adsorbed on the surface of CG-1 catalyst with respect to that observed in the previous spectrum recorded at 35 °C (Figure 12). Indeed, the adsorption and transformation of toluene was affected by the pre-adsorption of iPrOH at low temperature but in a reversible manner. This hypothesis is in agreement with the presence of toluene adsorption and toluene intermediate bands at 200 °C, such as those presented at 3060, 1300, 1180, 1080 cm^{-1} and notably, a more pronounced band at 1405 cm^{-1}, which is assigned to carboxylate species from toluene partial oxidation. Thus, the iPrOH was rapidly oxidized to acetone (or even totally oxidized to CO_2 and H_2O) at 200 °C, according to the less pronounced iPrOH adsorption bands (2969-2872, 1164 and 1124 cm^{-1}) and acetone bands (1337 and 1051 cm^{-1}), releasing catalyst active sites for toluene adsorption/oxidation or increasing the local temperature on catalyst surface, which would enhance the toluene oxidation. Moreover, a new band at 1550 cm^{-1}, which corresponds to stretching vibration of C=O in the benzoate species [51], could also be observed as well as the two bands at 2360 and 2330 cm^{-1} related to O=C=O group vibrations (not shown). This indicate that the deep oxidation of iPrOH and toluene likely takes place at this temperature.

Based on the above *in-situ* DRIFTS measurements, the pre-adsorption of toluene at low temperature clearly promotes the formation of formate or acetone intermediates species from iPrOH partial oxidation. This confirms the promotion effect induced by the presence of toluene. However, the pre-adsorption of iPrOH affects in a negative way the toluene adsorption and transformation at 35 ºC, but it was suppressed at 200 °C. Indeed, the toluene and intermediates species bands are clearly observed at this high temperature, suggesting that iPrOH is rapidly oxidize to acetone, releasing the catalyst active sites for toluene adsorption and oxidation or increasing the local temperature on catalyst surface. This is consistent with the shift of toluene conversion to lower temperatures in the light-off curves obtained in binary mixture.

4. Conclusions

Mn_2O_3 has been prepared by three different routes, citrate-gel (CG-1), P_{123} surfactant (P_{123}-1) and glycerol combustion (GM-1). CG-1 catalyst showed the highest catalytic activity for single and binary VOCs oxidation, which was notably attributed to the larger surface area (N_2-adsorprtion/desorption analyses), higher low-temperature reducibility and H_2 consumption (H_2-TPR measurements) and higher concentration of

surface-active oxygen species (XPS analysis). Furthermore, the catalytic results showed that the oxidation of these VOCs, when simultaneously introduced, differs from their single oxidation since the conversion of both toluene and iPrOH was shifted to lower temperatures in the binary mixture, suggesting a promoting effect. Moreover, the acetone in binary mixture was also obtained and completely oxidized at lower temperatures than in single oxidation, which could be attributed to the exothermic character induced by the oxidation of toluene and to a plausible promoting effect of a decrease of available oxygen on the selective iPrOH dehydrogenation reaction. In parallel, the toluene conversion, which starts when almost all iPrOH is completely oxidized, also shifted to lower temperatures under mixture conditions. This indicates that iPrOH, which is the more reactive VOC due to its higher polarity, initiates the oxidation reaction and promotes the oxidation of toluene by a local exothermicity.

The single toluene and iPrOH adsorption/oxidation as well as the catalytic oxidation of their binary mixture were investigated by *in-situ* DRIFTS. These measurements allowed to confirm the trends observed in the light-off curves and to understand the reaction mechanisms. While the main intermediates for toluene oxidation were the carboxylates (in particular benzoates species), acetone and formate were those mainly found for iPrOH oxidation. Besides, although some activity was observed in the absence of gaseous oxygen (notably due to catalyst chemisorbed or lattice oxygen), the adsorption of surface oxygen species from the gas phase was proved to be required to shift the VOCs conversion to lower temperatures and, in particular, the formation of highly oxidized products. These DRIFTS results also showed that the binary VOCs mixture oxidation strongly affects the intermediates formation temperature-dependency. Thus, the pre-adsorption of toluene over Mn_2O_3 catalyst had a promoting effect on iPrOH partial oxidation according to the increase of the bands attributed to the formation of formate or acetone intermediates species. On the other hand, although iPrOH pre-adsorption hindered the subsequent adsorption of toluene at low temperature due to the differences in the polarity of these VOCs, suggesting an inhibition effect on the toluene oxidation reaction, the co-feeding of both VOCs ultimately showed to be also beneficial for toluene conversion at high temperature. This could be attributed to the fast iPrOH conversion and the subsequent release of some catalyst active sites for toluene adsorption, along with the previously mentioned combustion-derived exothermic effect, which seemed to play a key role for both enhanced VOCs transformations.

5. Acknowledgements.

The authors gratefully acknowledge the scientific service and researchers of IRCELYON for the assistance in physico-chemical characterizations and for stimulating discussions and in particular to Pascale Mascunan, Yoann Aizac, Anne bonhomme, Laurence Burel and Pascal Bargiela.

6. References

[1] J. Zhu, W. Zhang, Q. Qi, H. Zhang, Y. Zhang, D. Sun, P. Liang, Catalytic oxidation of toluene, ethyl acetate and chlorobenzene over Ag/MnO2-cordierite molded catalyst, Sci. Rep. 9 (2019) 1–10. https://doi.org/10.1038/s41598-019-48506-5.

[2] P. Liu, Y. Liao, J. Li, L. Chen, M. Fu, P. Wu, R. Zhu, X. Liang, T. Wu, D. Ye, Insight into the effect of manganese substitution on mesoporous hollow spinel cobalt oxides for catalytic oxidation of toluene, J. Colloid Interface Sci. 594 (2021) 713–726. https://doi.org/10.1016/j.jcis.2021.03.093.

[3] C. Yang, G. Miao, Y. Pi, Q. Xia, J. Wu, Z. Li, J. Xiao, Abatement of various types of VOCs by adsorption/catalytic oxidation: A review, Chem. Eng. J. 370 (2019) 1128–1153. https://doi.org/https://doi.org/10.1016/j.cej.2019.03.232.

[4] C. He, J. Cheng, X. Zhang, M. Douthwaite, S. Pattisson, Z. Hao, Recent Advances in the Catalytic Oxidation of Volatile Organic Compounds: A Review Based on Pollutant Sorts and Sources, Chem. Rev. 119 (2019) 4471–4568. https://doi.org/10.1021/acs.chemrev.8b00408.

[5] X. Lai, X. Zhou, H. Zhang, X. Jiang, T. Lin, Y. Chen, Toluene oxidation over monolithic Mn x/ La-Al2O3 catalyst prepared by a CTAB-assisted impregnation method, Appl. Surf. Sci. 526 (2020) 146714. https://doi.org/10.1016/j.apsusc.2020.146714.

[6] W. Jedidi, J. Arfaoui, U. Caudillo-Flores, M.J. Muñoz-Batista, Z. Ksibi, A. Kubacka, A. Ghorbel, M. Fernández-García, Photodegradation of 2-propanol in gas phase over zirconium doped TiO2: Effect of Zr content, J. Photochem. Photobiol. A Chem. 427 (2022). https://doi.org/10.1016/j.jphotochem.2022.113774.

[7] Y. Guo, M. Wen, G. Li, T. An, Recent advances in VOC elimination by catalytic oxidation technology onto various nanoparticles catalysts : a critical review, Appl. Catal. B Environ. 281 (2021) 119447. https://doi.org/10.1016/j.apcatb.2020.119447.

[8] P. Kleemola-Juntunen, S. Kirchner, Gothenburg Protocol and Convention on Long-Range Transboundary Air Pollution BT - Global Encyclopedia of Territorial Rights, in: K.W. Gray (Ed.), Springer International Publishing, Cham, 2020: pp. 1–8. https://doi.org/10.1007/978-3-319-68846-6_15-2.

[9] Y.S. Son, Decomposition of VOCs and odorous compounds by radiolysis: A critical review, Chem. Eng. J. 316 (2017) 609–622. https://doi.org/10.1016/j.cej.2017.01.063.

[10] Y. Liu, X. Feng, D. Lawless, Separation of gasoline vapor from nitrogen by hollow fiber composite membranes for VOC emission control, J. Memb. Sci. 271 (2006) 114–124. https://doi.org/10.1016/j.memsci.2005.07.012.

[11] F.I. Khan, A. Kr. Ghoshal, Removal of Volatile Organic Compounds from polluted air, J. Loss Prev. Process Ind. 13 (2000) 527–545. https://doi.org/https://doi.org/10.1016/S0950-4230(00)00007-3.

[12] G.R. Parmar, N.N. Rao, Emerging Control Technologies for Volatile Organic Compounds, Crit. Rev. Environ. Sci. Technol. 39 (2008) 41–78. https://doi.org/10.1080/10643380701413658.

[13] Z. Zhang, Z. Jiang, W. Shangguan, Low-temperature catalysis for VOCs removal in technology and application: A state-of-the-art review, Catal. Today. 264 (2016) 270–278. https://doi.org/10.1016/j.cattod.2015.10.040.

[14] W. Tang, G. Liu, D. Li, H. Liu, X. Wu, N. Han, Y. Chen, Design and synthesis of porous non-noble metal oxides for catalytic removal of VOCs, Sci. China Chem. 58 (2015) 1359–1366. https://doi.org/10.1007/s11426-015-5469-8.

[15] L.F. Liotta, Catalytic oxidation of volatile organic compounds on supported noble metals, Appl. Catal. B Environ. 100 (2010) 403–412. https://doi.org/10.1016/j.apcatb.2010.08.023.

[16] Z. Wang, S. Li, S. Xie, Y. Liu, H. Dai, G. Guo, J. Deng, Supported ultralow loading Pt catalysts with high H2O- , CO2- , and SO2- resistance for acetone removal, Appl. Catal. A, Gen. 579 (2019) 106–115. https://doi.org/10.1016/j.apcata.2019.04.018.

[17] A. Musialik-Piotrowska, B. Mendyka, Catalytic oxidation of chlorinated hydrocarbons in two-component mixtures with selected VOCs, in: Catal. Today, 2004: pp. 139–144. https://doi.org/10.1016/j.cattod.2004.04.019.

[18] Y. Huang, B. Long, M. Tang, Z. Rui, M.S. Balogun, Y. Tong, H. Ji, Bifunctional catalytic material: An ultrastable and high-performance surface defect CeO2 nanosheets for formaldehyde thermal oxidation and photocatalytic oxidation, Appl. Catal. B Environ. 181 (2016) 779–787. https://doi.org/10.1016/j.apcatb.2015.08.047.

[19] Y. Wang, A. Zhu, B. Chen, M. Crocker, C. Shi, Three-dimensional ordered

mesoporous Co-Mn oxide: A highly active catalyst for “storage-oxidation” cycling for the removal of formaldehyde, Catal. Commun. 36 (2013) 52–57. https://doi.org/10.1016/j.catcom.2013.03.007.

[20] Y. Wang, L. Zhang, L. Guo, Enhanced Toluene Combustion over Highly Homogeneous Iron Manganese Oxide Nanocatalysts, ACS Appl. Nano Mater. 1 (2018) 1066–1075. https://doi.org/10.1021/acsanm.7b00258.

[21] C. Shi, Y. Wang, A. Zhu, B. Chen, C. Au, Mn xCo 3 - XO 4 solid solution as high-efficient catalysts for low-temperature oxidation of formaldehyde, Catal. Commun. 28 (2012) 18–22. https://doi.org/10.1016/j.catcom.2012.08.003.

[22] J. González-Cobos, B. Mylonoyannis, G. Chai, W. Zhang, C. Tian, A. Kaddouri, S. Gil, Low-temperature gas-phase toluene catalytic combustion over modified CoCr2O4 spinel catalysts: Effect of Co/Cr content and calcination temperature, Appl. Catal. A Gen. 657 (2023) 119162. https://doi.org/https://doi.org/10.1016/j.apcata.2023.119162.

[23] Z. Sihaib, F. Puleo, J.M. Garcia-Vargas, L. Retailleau, C. Descorme, L.F. Liotta, J.L. Valverde, S. Gil, A. Giroir-Fendler, Manganese oxide-based catalysts for toluene oxidation, Appl. Catal. B Environ. 209 (2017). https://doi.org/10.1016/j.apcatb.2017.03.042.

[24] X. Zhang, J. Zhao, Z. Song, W. Liu, H. Zhao, M. Zhao, Y. Xing, Z. Ma, H. Du, The catalytic oxidation performance of toluene over the Ce-Mn-Ox catalysts: Effect of synthetic routes, J. Colloid Interface Sci. 562 (2020) 170–181. https://doi.org/10.1016/j.jcis.2019.12.029.

[25] Z. Ye, J.M. Giraudon, N. Nuns, P. Simon, N. De Geyter, R. Morent, J.F. Lamonier, Influence of the preparation method on the activity of copper-manganese oxides for toluene total oxidation, Appl. Catal. B Environ. 223 (2018) 154–166. https://doi.org/10.1016/j.apcatb.2017.06.072.

[26] Z. Wang, P. Ma, K. Zheng, C. Wang, Y. Liu, H. Dai, C. Wang, H.C. Hsi, J. Deng, Size effect, mutual inhibition and oxidation mechanism of the catalytic removal of a toluene and acetone mixture over TiO2 nanosheet-supported Pt nanocatalysts, Appl. Catal. B Environ. 274 (2020) 118963. https://doi.org/10.1016/j.apcatb.2020.118963.

[27] V. Blasin-Aubé, J. Belkouch, L. Monceaux, General study of catalytic oxidation of various VOCs over La0.8Sr0.2MnO3+x perovskite catalyst—influence of mixture, Appl. Catal. B Environ. 43 (2003) 175–186.

https://doi.org/https://doi.org/10.1016/S0926-3373(02)00302-8.

[28] C. He, P. Li, J. Cheng, Z.P. Hao, Z.P. Xu, A comprehensive study of deep catalytic oxidation of benzene, toluene, ethyl acetate, and their mixtures over Pd/ZSM-5 catalyst: Mutual effects and kinetics, Water. Air. Soil Pollut. 209 (2010) 365–376. https://doi.org/10.1007/s11270-009-0205-7.

[29] N. Burgos, M. Paulis, M. Mirari Antxustegi, M. Montes, Deep oxidation of VOC mixtures with platinum supported on Al2O3/Al monoliths, Appl. Catal. B Environ. 38 (2002) 251–258. https://doi.org/https://doi.org/10.1016/S0926-3373(01)00294-6.

[30] R. Beauchet, P. Magnoux, J. Mijoin, Catalytic oxidation of volatile organic compounds (VOCs) mixture (isopropanol/o-xylene) on zeolite catalysts, Catal. Today. 124 (2007) 118–123. https://doi.org/10.1016/j.cattod.2007.03.030.

[31] T. Pan, H. Deng, Y. Lu, J. Ma, L. Wang, C. Zhang, H. He, Synergistic Catalytic Oxidation of Typical Volatile Organic Compound Mixtures on Mn-Based Catalysts: Significant Promotion Effect and Reaction Mechanism, Environ. Sci. Technol. 57 (2023) 1123–1133. https://doi.org/10.1021/acs.est.2c06514.

[32] F.N. Aguero, B.P. Barbero, L. Gambaro, L.E. Cadús, Catalytic combustion of volatile organic compounds in binary mixtures over MnOx/Al2O3 catalyst, Appl. Catal. B Environ. 91 (2009) 108–112. https://doi.org/10.1016/j.apcatb.2009.05.012.

[33] P. Papaefthimiou, T. Ioannides, X.E. Verykios, Performance of doped Pt/TiO2 (W6+) catalysts for combustion of volatile organic compounds (VOCS), Appl. Catal. B Environ. 15 (1998) 75–92. https://doi.org/10.1016/S0926-3373(97)00038-6.

[34] S. Ordóñez, L. Bello, H. Sastre, R. Rosal, F. V. Díez, Kinetics of the deep oxidation of benzene, toluene, n-hexane and their binary mixtures over a platinum on γ-alumina catalyst, Appl. Catal. B Environ. 38 (2002) 139–149. https://doi.org/10.1016/S0926-3373(02)00036-X.

[35] A. Musialik-Piotrowska, K. Syczewska, Combustion of volatile organic compounds in two-component mixtures over monolithic perovskite catalysts, Catal. Today. 59 (2000) 269–278. https://doi.org/https://doi.org/10.1016/S0920-5861(00)00293-5.

[36] B. Bassou, N. Guilhaume, E.E. Iojoiu, D. Farrusseng, K. Lombaert, D. Bianchi, C. Mirodatos, High-throughput approach to the catalytic combustion of diesel

soot II: Screening of oxide-based catalysts, Catal. Today. 159 (2011) 138–143. https://doi.org/10.1016/j.cattod.2010.05.042.

[37] A.S. Poyraz, W. Song, D. Kriz, C. Kuo, M.S. Seraji, S.L. Suib, Crystalline Mesoporous K2−xMn8O16 and ε‐ MnO2 by Mild Transformations of Amorphous Mesoporous Manganese Oxides and Their Enhanced Redox Properties, ACS Appl. Mater. Interfaces. 6 (2014) 10986–10991.

[38] C. Coudercy, V. L'hospital, R. Checa, A. Le Valant, P. Afanasiev, S. Loridant, On the reaction mechanism of MnOx/SAPO-34 bifunctional catalysts for the conversion of syngas to light olefins, Catal. Sci. Technol. 11 (2021) 7844–7849. https://doi.org/10.1039/d1cy01673c.

[39] X. Yu, B. Deng, L. Yang, M. Zou, Z. Chen, Y. Fan, Z. Wei, K. Chen, M. Lu, T. Ying, J. Zhang, W. Dai, Influence of residual anions (Cl-, SO42-and NO3-) on Mn2O3for photothermal catalytic oxidation of toluene, J. Environ. Chem. Eng. 10 (2022) 108496. https://doi.org/10.1016/j.jece.2022.108496.

[40] P. Gong, J. Xie, D. Fang, F. He, F. Li, K. Qi, Study on the relationship between physicochemical properties and catalytic activity of Mn2O3 nanorods, Mater. Res. Express. 4 (2017). https://doi.org/10.1088/2053-1591/aa9a25.

[41] S. Xie, J. Deng, Y. Liu, Z. Zhang, H. Yang, Y. Jiang, H. Arandiyan, H. Dai, C.T. Au, Excellent catalytic performance, thermal stability, and water resistance of 3DOM Mn2O3-supported Au-Pd alloy nanoparticles for the complete oxidation of toluene, Appl. Catal. A Gen. 507 (2015) 82–90. https://doi.org/10.1016/j.apcata.2015.09.026.

[42] J. Wang, H. Zhao, J. Song, T. Zhu, W. Xu, Structure-Activity Relationship of Manganese Oxide Catalysts for the Catalytic Oxidation of (chloro)-VOCs, Catalysts. 9 (2019). https://doi.org/10.3390/catal9090726.

[43] X. Chen, X. Chen, S. Cai, E. Yu, J. Chen, H. Jia, MnOx/Cr2O3 composites prepared by pyrolysis of Cr-MOF precursors containing in situ assembly of MnOx as high stable catalyst for toluene oxidation, Appl. Surf. Sci. 475 (2019) 312–324. https://doi.org/https://doi.org/10.1016/j.apsusc.2018.12.277.

[44] F. Wang, H. Dai, J. Deng, G. Bai, K. Ji, Y. Liu, Manganese Oxides with Rod-, Wire-, Tube-, and Flower-Like Morphologies: Highly Effective Catalysts for the Removal of Toluene, Environ. Sci. Technol. 46 (2012) 4034–4041. https://doi.org/10.1021/es204038j.

[45] X. Zhang, H. Zhao, Z. Song, W. Liu, J. Zhao, Z. Ma, M. Zhao, Y. Xing, Insight

into the effect of oxygen species and Mn chemical valence over MnOx on the catalytic oxidation of toluene, Appl. Surf. Sci. 493 (2019) 9–17. https://doi.org/10.1016/j.apsusc.2019.06.255.

[46] N.D. Wasalathanthri, A.S. Poyraz, S. Biswas, Y. Meng, C.H. Kuo, D.A. Kriz, S.L. Suib, High-performance catalytic CH4 oxidation at low temperatures: Inverse micelle synthesis of amorphous mesoporous manganese oxides and mild transformation to K2- xMn8O16 and μ-MnO2, J. Phys. Chem. C. 119 (2015) 1473–1482. https://doi.org/10.1021/jp5108558.

[47] B. Bai, J. Li, J. Hao, 1D-MnO2, 2D-MnO2 and 3D-MnO2 for low-temperature oxidation of ethanol, Appl. Catal. B Environ. 164 (2015) 241–250. https://doi.org/https://doi.org/10.1016/j.apcatb.2014.08.044.

[48] S. Todorova, J.L. Blin, A. Naydenov, B. Lebeau, H. Kolev, P. Gaudin, A. Dotzeva, R. Velinova, D. Filkova, I. Ivanova, L. Vidal, L. Michelin, L. Josien, K. Tenchev, Co3O4-MnOx oxides supported on SBA-15 for CO and VOCs oxidation, Catal. Today. 357 (2020) 602–612. https://doi.org/https://doi.org/10.1016/j.cattod.2019.05.018.

[49] J. Jia, P. Zhang, L. Chen, Catalytic decomposition of gaseous ozone over manganese dioxides with different crystal structures, Appl. Catal. B Environ. 189 (2016) 210–218. https://doi.org/https://doi.org/10.1016/j.apcatb.2016.02.055.

[50] C. Dong, Z. Qu, X. Jiang, Y. Ren, Tuning oxygen vacancy concentration of MnO2 through metal doping for improved toluene oxidation, J. Hazard. Mater. 391 (2020) 122181. https://doi.org/10.1016/j.jhazmat.2020.122181.

[51] X. Yang, X. Yu, M. Lin, X. Ma, M. Ge, Enhancement effect of acid treatment on Mn2O3catalyst for toluene oxidation, Catal. Today. (2018) 0–1. https://doi.org/10.1016/j.cattod.2018.04.041.

[52] M. Wang, L. Zhang, W. Huang, Y. Zhou, H. Zhao, J. Lv, J. Tian, X. Kan, J. Shi, Pt/MnO2 nanosheets: facile synthesis and highly efficient catalyst for ethylene oxidation at low temperature, RSC Adv. 7 (2017) 14809–14815. https://doi.org/10.1039/C6RA26529D.

[53] M.H. Castaño, R. Molina, S. Moreno, Cooperative effect of the Co–Mn mixed oxides for the catalytic oxidation of VOCs: Influence of the synthesis method, Appl. Catal. A Gen. 492 (2015) 48–59. https://doi.org/https://doi.org/10.1016/j.apcata.2014.12.009.

[54] L. Zhang, S. Wang, L. Lv, Y. Ding, D. Tian, S. Wang, Insights into the roles of

surface oxygen species of manganese oxides for the ozone elimination at ambient temperature, Authorea. (2020). https://doi.org/10.22541/au.158888524.46953074.

[55] P. Mars, D.W. van Krevelen, Oxidations carried out by means of vanadium oxide catalysts, Chem. Eng. Sci. 3 (1954) 41–59. https://doi.org/https://doi.org/10.1016/S0009-2509(54)80005-4.

[56] Q. Zhao, Q. Liu, Y. Zheng, R. Han, C. Song, N. Ji, D. Ma, Enhanced catalytic performance for volatile organic compound oxidation over in-situ growth of MnOx on Co3O4 nanowire, Chemosphere. 244 (2020). https://doi.org/10.1016/j.chemosphere.2019.125532.

[57] S.I. Suárez-Vázquez, E.J. Moreno-Román, R. Zanella, A. Cruz-López, C. García-Goméz, A. Nieto-Márquez, S. Gil, Insight into the surface reaction mechanism of toluene oxidation over a composite CeOx/La1-xCexMnO3 catalyst using DRIFTS, Chem. Eng. Sci. 259 (2022). https://doi.org/10.1016/j.ces.2022.117831.

[58] B. Zhou, K. Xi, L.J. Fan, Y. Zhou, Y. Wang, Q.L. Zhu, H.F. Lu, A comparative study on Ce–Pr and Ce–Mn mixed oxide catalysts toward soot catalytic combustion, Appl. Catal. A Gen. 562 (2018) 1–10. https://doi.org/10.1016/j.apcata.2018.05.034.

[59] S. Mo, Q. Zhang, J. Li, Y. Sun, Q. Ren, S. Zou, Q. Zhang, J. Lu, M. Fu, D. Mo, J. Wu, H. Huang, D. Ye, Highly efficient mesoporous MnO2 catalysts for the total toluene oxidation: Oxygen-Vacancy defect engineering and involved intermediates using in situ DRIFTS, Appl. Catal. B Environ. 264 (2020) 118464. https://doi.org/https://doi.org/10.1016/j.apcatb.2019.118464.

[60] X. Yang, X. Yu, M. Lin, X. Ma, M. Ge, Enhancement effect of acid treatment on Mn2O3 catalyst for toluene oxidation, Catal. Today. 327 (2019) 254–261. https://doi.org/https://doi.org/10.1016/j.cattod.2018.04.041.

[61] Y. Luo, Y.-Q. Deng, W. Mao, X.-J. Yang, K. Zhu, J. Xu, Y.-F. Han, Probing the Surface Structure of α-Mn2O3 Nanocrystals during CO Oxidation by Operando Raman Spectroscopy, J. Phys. Chem. C. 116 (2012) 20975–20981. https://doi.org/10.1021/jp307637w.

[62] R. Naeem, M. Ali Ehsan, R. Yahya, M. Sohail, H. Khaledi, M. Mazhar, Fabrication of pristine Mn2O3 and Ag–Mn2O3 composite thin films by AACVD for photoelectrochemical water splitting, Dalt. Trans. 45 (2016) 14928–14939. https://doi.org/10.1039/C6DT02656G.

[63] D. Li, Q. Yu, S.-S. Li, H.-Q. Wan, L.-J. Liu, L. Qi, B. Liu, F. Gao, L. Dong, Y. Chen, The Remarkable Enhancement of CO-Pretreated CuO□Mn2O3/γ-Al2O3 Supported Catalyst for the Reduction of NO with CO: The Formation of Surface Synergetic Oxygen Vacancy, Chem. – A Eur. J. 17 (2011) 5668–5679. https://doi.org/https://doi.org/10.1002/chem.201002786.

[64] J. Waikar, P. More, Complete oxidation of CO and propene as model component of diesel exhaust and VOC using manganese oxide supported on octahedral (AlO63−)-Ce3+, Appl. Surf. Sci. Adv. 7 (2022) 100204. https://doi.org/https://doi.org/10.1016/j.apsadv.2021.100204.

[65] P. Wang, J. Wang, J. Zhao, X. Ma, X. Du, S. Peng, X. Hao, B. Tang, A. Abudula, G. Guan, Trace holmium assisting delaminated OMS-2 catalysts for total toluene oxidation at low temperature, J. Colloid Interface Sci. (2021). https://doi.org/10.1016/j.jcis.2021.10.077.

[66] W. Yang, Y. Zhu, F. You, L. Yan, Y. Ma, C. Lu, P. Gao, Q. Hao, W. Li, Insights into the surface-defect dependence of molecular oxygen activation over birnessite-type MnO2, Appl. Catal. B Environ. 233 (2018) 184–193. https://doi.org/https://doi.org/10.1016/j.apcatb.2018.03.107.

[67] L. Wang, T. Wen, H. Dong, J. Zhang, C. Long, Selective catalytic ozonation of gaseous ammonia to dinitrogen on cryptomelane-type manganese oxide catalysts: Role of oxygen vacancies and acid sites, J. Clean. Prod. 343 (2022) 130906. https://doi.org/https://doi.org/10.1016/j.jclepro.2022.130906.

[68] C. He, Y. Wang, Z. Li, Y. Huang, Y. Liao, D. Xia, S. Lee, Facet Engineered α-MnO2 for Efficient Catalytic Ozonation of Odor CH3SH: Oxygen Vacancy-Induced Active Centers and Catalytic Mechanism, Environ. Sci. Technol. 54 (2020) 12771–12783. https://doi.org/10.1021/acs.est.0c05235.

[69] R. Cao, L. Li, P. Zhang, L. Gao, S. Rong, Regulating oxygen vacancies in ultrathin δ-MnO2 nanosheets with superior activity for gaseous ozone decomposition, Environ. Sci. Nano. 8 (2021) 1628–1641. https://doi.org/10.1039/D1EN00149C.

[70] J. Chen, X. Chen, W. Xu, Z. Xu, J. Chen, H. Jia, J. Chen, Hydrolysis driving redox reaction to synthesize Mn-Fe binary oxides as highly active catalysts for the removal of toluene, Chem. Eng. J. 330 (2017) 281–293. https://doi.org/https://doi.org/10.1016/j.cej.2017.07.147.

[71] J. Du, Z. Qu, C. Dong, L. Song, Y. Qin, N. Huang, Low-temperature abatement

of toluene over Mn-Ce oxides catalysts synthesized by a modified hydrothermal approach, Appl. Surf. Sci. 433 (2018) 1025–1035. https://doi.org/10.1016/j.apsusc.2017.10.116.

[72] X. Zhang, H. Zhao, Z. Song, W. Liu, J. Zhao, Z. Ma, M. Zhao, Y. Xing, Insight into the effect of oxygen species and Mn chemical valence over MnOx on the catalytic oxidation of toluene, Appl. Surf. Sci. 493 (2019) 9–17. https://doi.org/https://doi.org/10.1016/j.apsusc.2019.06.255.

[73] J. Zhou, L. Qin, W. Xiao, C. Zeng, N. Li, T. Lv, H. Zhu, Oriented growth of layered-MnO2 nanosheets over α-MnO2 nanotubes for enhanced room-temperature HCHO oxidation, Appl. Catal. B Environ. 207 (2017) 233–243. https://doi.org/https://doi.org/10.1016/j.apcatb.2017.01.083.

[74] C. Zhou, H. Zhang, Z. Zhang, L. Li, Improved reactivity for toluene oxidation on MnO x / CeO 2 -ZrO 2 catalyst by the synthesis of cubic-tetragonal interfaces, Appl. Surf. Sci. 539 (2021) 148188. https://doi.org/10.1016/j.apsusc.2020.148188.

[75] S.Y. Liu, S.M. Yang, Complete oxidation of 2-propanol over gold-based catalysts supported on metal oxides, Appl. Catal. A Gen. 334 (2008) 92–99. https://doi.org/https://doi.org/10.1016/j.apcata.2007.09.037.

[76] J. Kubo, W. Ueda, Catalytic behavior of AMoOx (A = Ba, Sr) in oxidation of 2-propanol, Mater. Res. Bull. 44 (2009) 906–912. https://doi.org/10.1016/j.materresbull.2008.08.013.

[77] X. Tang, J. Li, L. Sun, J. Hao, Origination of N2O from NO reduction by NH3 over β-MnO2 and α-Mn2O3, Appl. Catal. B Environ. 99 (2010) 156–162. https://doi.org/https://doi.org/10.1016/j.apcatb.2010.06.012.

[78] S. Dissanayake, N. Wasalathanthri, A. Shirazi Amin, J. He, S. Poges, D. Rathnayake, S.L. Suib, Mesoporous Co3O4 catalysts for VOC elimination: Oxidation of 2-propanol, Appl. Catal. A Gen. 590 (2020). https://doi.org/10.1016/j.apcata.2019.117366.

[79] B. Levasseur, S. Kaliaguine, Effects of iron and cerium in La1-yCeyCo1-xFexO3 perovskites as catalysts for VOC oxidation, Appl. Catal. B Environ. 88 (2009) 305–314. https://doi.org/10.1016/j.apcatb.2008.11.007.

[80] M. Lu, R. Huang, W. Xu, J. Wu, M. Fu, L. Chen, D. Ye, Competitive Adsorption of O2 and Toluene on the Surface of FeOx/SBA-15 Catalyst, Aerosol Air Qual. Res. 17 (2017) 2310–2316. https://doi.org/10.4209/aaqr.2016.05.0186.

[81] W. Xu, D. Raftery, J.S. Francisco, Effect of Irradiation Sources and Oxygen Concentration on the Photocatalytic Oxidation of 2-Propanol and Acetone Studied by in Situ FTIR, J. Phys. Chem. B. 107 (2003) 4537–4544. https://doi.org/10.1021/jp025995h.

[82] T. Yan, J. Gong, C.B. Mullins, Oxygen Exchange in the Selective Oxidation of 2-Butanol on Oxygen Precovered Au(111), J. Am. Chem. Soc. 131 (2009) 16189–16194. https://doi.org/10.1021/ja9062986.

[83] Y. Lyu, C. Li, X. Du, Y. Zhu, Y. Zhang, S. Li, Catalytic oxidation of toluene over MnO2 catalysts with different Mn (II) precursors and the study of reaction pathway, Fuel. 262 (2019) 116610. https://doi.org/10.1016/j.fuel.2019.116610.

[84] J.J. Li, E.Q. Yu, S.C. Cai, X. Chen, J. Chen, H.P. Jia, Y.J. Xu, Noble metal free, CeO2/LaMnO3hybrid achieving efficient photo-thermal catalytic decomposition of volatile organic compounds under IR light, Appl. Catal. B Environ. 240 (2019) 141–152. https://doi.org/10.1016/j.apcatb.2018.08.069.

[85] Z. Wang, S. Xie, Y. Feng, P. Ma, K. Zheng, E. Duan, Y. Liu, H. Dai, J. Deng, Simulated solar light driven photothermal catalytic purification of toluene over iron oxide supported single atom Pt catalyst, Appl. Catal. B Environ. 298 (2021) 120612. https://doi.org/10.1016/j.apcatb.2021.120612.

[86] P. Wang, J. Zhao, Q. Zhao, X. Ma, X. Du, X. Hao, B. Tang, A. Abudula, G. Guan, Microwave-assisted synthesis of manganese oxide catalysts for total toluene oxidation, J. Colloid Interface Sci. 607 (2022) 100–110. https://doi.org/10.1016/j.jcis.2021.08.170.

[87] M.G. Jeong, E.J. Park, H.O. Seo, K.D. Kim, Y.D. Kim, D.C. Lim, Humidity effect on photocatalytic activity of TiO 2 and regeneration of deactivated photocatalysts, Appl. Surf. Sci. 271 (2013) 164–170. https://doi.org/10.1016/j.apsusc.2013.01.155.

[88] X. Zhang, L. Song, F. Bi, D. Zhang, Y. Wang, L. Cui, Catalytic oxidation of toluene using a facile synthesized Ag nanoparticle supported on UiO-66 derivative, J. Colloid Interface Sci. (2020). https://doi.org/10.1016/j.jcis.2020.03.031.

[89] Y. Xu, Z. Qu, Y. Ren, C. Dong, Enhancement of toluene oxidation performance over Cu – Mn composite oxides by regulating oxygen vacancy, Appl. Surf. Sci. 560 (2021) 149983.

[90] H. Sun, Z. Liu, S. Chen, X. Quan, The role of lattice oxygen on the activity and

selectivity of the OMS-2 catalyst for the total oxidation of toluene, Chem. Eng. J. 270 (2015) 58–65. https://doi.org/10.1016/j.cej.2015.02.017.

[91] J. Lichtenberger, M.D. Amiridis, Catalytic oxidation of chlorinated benzenes over V 2 O 5 / TiO 2 catalysts, J. Catal. 223 (2004) 296–308. https://doi.org/10.1016/j.jcat.2004.01.032.

[92] J. Zhong, Y. Zeng, M. Zhang, W. Feng, D. Xiao, J. Wu, Toluene oxidation process and proper mechanism over Co 3 O 4 nanotubes : Investigation through in-situ DRIFTS combined with PTR-TOF-MS and quasi in-situ XPS, Chem. Eng. J. 397 (2020) 125375. https://doi.org/10.1016/j.cej.2020.125375.

[93] X. Yang, X. Yu, M. Jing, W. Song, J. Liu, M. Ge, Defective Mn x Zr 1 − x O 2 Solid Solution for the Catalytic Oxidation of Toluene : Insights into the Oxygen Vacancy Contribution, ACS Appl. Mater. Interfaces. 11 (2019) 730–739. https://doi.org/10.1021/acsami.8b17062.

[94] X. Li, Z. Zhu, Q. Zhao, S. Liu, FT-IR study of the photocatalytic degradation of gaseous toluene over UV-irradiated TiO 2 microballs : enhanced performance by hydrothermal treatment in alkaline solution, Appl. Surf. Sci. 257 (2011) 4709–4714. https://doi.org/10.1016/j.apsusc.2010.12.133.

[95] J. Lu, J. Zhong, Q. Ren, J. Li, L. Song, S. Mo, M. Zhang, P. Chen, M. Fu, D. Ye, Construction of Cu-Ce interface for boosting toluene oxidation : Study of Cu-Ce interaction and intermediates identified by in situ DRIFTS, Chinese Chem. Lett. (2021) 6372. https://doi.org/10.1016/j.cclet.2021.05.029.

[96] C. Barakat, P. Gravejat, O. Guaitella, F. Thevenet, A. Rousseau, Oxidation of isopropanol and acetone adsorbed on TiO2 under plasma generated ozone flow: Gas phase and adsorbed species monitoring, Appl. Catal. B Environ. 147 (2014) 302–313. https://doi.org/10.1016/j.apcatb.2013.09.008.

[97] H. Zhang, L. Dai, Y. Feng, Y. Xu, Y. Liu, G. Guo, J. Deng, A Resource utilization method for volatile organic compounds emission from the semiconductor industry : Selective catalytic oxidation of isopropanol to acetone Over Au / α-Fe 2 O 3 nanosheets, Appl. Catal. B Environ. 275 (2020) 119011. https://doi.org/10.1016/j.apcatb.2020.119011.

[98] F.M. Bkangmo Kontchouo, K. Sun, C. Li, Z. Fu, S. Zhang, L. Xu, X. Hu, Steam reforming of acetone and isopropanol : Investigation of correlation of ketone and alcohol functional groups with properties of coke, J. Energy Inst. 101 (2022) 32–44. https://doi.org/10.1016/j.joei.2021.12.001.

[99] E. Omari, M. Omari, D. Barkat, Oxygen evolution reaction over copper and zinc co-doped LaFeO3perovskite oxides, Polyhedron. 156 (2018) 116–122. https://doi.org/10.1016/j.poly.2018.09.031.

[100] J. Zhong, Y. Zeng, D. Chen, S. Mo, M. Zhang, M. Fu, J. Wu, Z. Su, P. Chen, D. Ye, Toluene oxidation over Co3+-rich spinel Co3O4: Evaluation of chemical and by-product species identified by in situ DRIFTS combined with PTR-TOF-MS, J. Hazard. Mater. 386 (2020) 121957. https://doi.org/https://doi.org/10.1016/j.jhazmat.2019.121957.

[101] M. Aghbolaghy, J. Soltan, N. Chen, Low Temperature Catalytic Oxidation of Binary Mixture of Toluene and Acetone in the Presence of Ozone, Catal. Letters. 0 (2018) 0. https://doi.org/10.1007/s10562-018-2536-8.

Tables caption

Table 1. Structural and textural properties of Mn_2O_3 catalysts synthetized by Citrate-Gel (CG-1), P_{123} surfactant (P_{123}-1) and Glycerol precipitation (GM-1) methods.

Table 2. Redox and surface properties of synthetized Mn_2O_3 oxides-based catalysts obtained by H_2-TPR and XPS measurements.

Table 3. Comparison of catalytic activity for toluene oxidation.

Table 4. Comparison of catalytic activity for single iPrOH catalytic oxidation.

Table 5. Catalytic activity comparison for single VOC and binary mixture oxidation over the three Mn_2O_3 oxides-based catalysts synthetized in the present work.

Table 6. Main bands of toluene oxidation intermediates.

Table 7. Main bands of iPrOH intermediates.

Table 1. Structural and textural properties of Mn_2O_3 catalysts synthetized by Citrate-Gel (CG-1), P_{123} surfactant (P_{123}-1) and Glycerol precipitation (GM-1) methods.

Catalyst	Main phase	Crystallite size (nm)	S_{BET} (m^2g^{-1})	Total pore volume ($cm^3\ g^{-1}$)	Mean pore size (nm)
CG-1	Cubic Mn_2O_3	26	24	0.11	22
P_{123}-1	Cubic Mn_2O_3	39	9	0.06	22
GM-1	Cubic Mn_2O_3	30	19	0.11	22

Table 2. Redox and surface properties of synthetized Mn_2O_3 oxides-based catalysts obtained by H_2-TPR and XPS measurements.

	H_2-TPR	**XPS**		
Catalyst	**H_2 consumption (mmol H_2 g^{-1})**	**O/Mn**	**O_{ads}/O_{latt}**	**Mn^{3+}/Mn^{4+}**
CG-1	9.1	1.6	0.39	2.79
P_{123}-1	6.3	1.2	0.29	1.65
GM-1	5.7	1.4	0.32	2.12

Table 3. Comparison of catalytic activity for toluene oxidation.

Catalyst	T_{25} conversion (°C)	T_{50} conversion (°C)	T_{90} conversion (°C)	Reaction rate (μmol g^{-1} s^{-1}) at 290 °C	Specific reaction rate (μmol m^{-2} s^{-1}) at 290 °C
CG-1	291	310	337	1.39	0.058
P_{123}-1	315	336	373	0.65	0.072
GM-1	298	318	348	1.33	0.067

Table 4. Comparison of catalytic activity for single iPrOH catalytic oxidation.

Catalyst	T_{25} conversion (°C)	T_{50} conversion (°C)	T_{90} conversion (°C)	Reaction rate (µmol g^{-1} s^{-1}) at 120 °C	Specific reaction rate (µmol m^{-2} s^{-1}) at 120 °C
CG-1	125	146	237	1.38	0.050
P_{123}-1	175	213	259	0.58	0.081
GM-1	118	179	232	1.64	0.070

Table 5. Catalytic activity comparison for single VOC and binary mixture oxidation over the three Mn_2O_3 oxides-based catalysts synthetized in the present work.

Catalyst	Single VOC oxidation				Mixture VOCs oxidation			
	T_{50} Toluene (°C)	T_{90} Toluene (°C)	T_{50} iPrOH (°C)	T_{90} iPrOH (°C)	T_{50} Toluene (°C)	T_{90} Toluene (°C)	T_{50} iPrOH (°C)	T_{90} iPrOH (°C)
CG-1	310	337	146	238	291	316	107	217
P_{123}-1	336	373	213	258	330	360	162	229
GM-1	318	348	179	232	303	327	142	217

Table 6. Main bands of toluene oxidation intermediates.

Position (cm^{-1})	Assignment	Reference
	Toluene adsorption bands	
3060-2870	ν_sC-H aromatic ring	[83–85]
1600	ν_sC-H aromatic ring	[85]
1494	ν_sC-H aromatic ring	[83,85]
1026	ν_sC-H aromatic ring	[86]
1291	$\nu_a CH_3$	[74]
	Toluene reaction intermediates	
1963 - 1816	υC=O, maleic anhydrides	[92,93]
1692	υC=O, quinone or ketone species	[92,100,101]
1591, 1462	υC=O, aldehyde species	[74,94]
1448	υCOO-, acetate species	[91]
1569 -1403	υC=O, carboxylate species	[51]
1405 - 1384	υC=O, carboxylate species	[83]
1300, 1337	υC=O, maleic anhydrides	[89,90]
1150-1000	νCO-, alkoxide species or benzyl alcohol	[65,87]
1180	υC-O, benzoic acid	[65]

Table 7. Main bands of iPrOH intermediates.

Position (cm^{-1})	Assignment	Reference
iPrOH adsorption bands		
2982-2872	ν_sC-H	[96]
1468, 1384, 1215, 1164, 1124	νCH_3, δC-C, isopropoxide species	[96–98]
1290	δO-H	[97]
iPrOH reaction intermediates		
1569	ν_aCOO, formate species	[98]
1437	νC=C, acetone enol form	[98]
1337	νC-C, acetone	[96,98]
1419, 1051	δCH_3, acetone	[16,96,98]

Figures caption

Figure 1. XRD diffractograms of the synthetized Mn_2O_3 catalysts by Citrate-Gel (CG-1), P_{123} surfactant (P_{123}-1) and Glycerol precipitation (GM-1) preparation methods.

Figure 2. a) H_2-TPR and b) O_2-TPD profiles of Mn_2O_3 catalysts prepared by Citrate-Gel, P_{123} surfactant and glycerol precipitation methods. The inset of Figure 2b shows the oxygen desorption in the temperature range corresponding with physisorbed and chemisorbed oxygen species.

Figure 3. High-resolution XPS results for Mn_2O_3 catalysts; a) Mn 3*s*, b) Mn 2*p* and c) O 1*s*.

Figure 4. Single toluene catalytic oxidation over the Mn_2O_3 catalysts synthetized by different preparation methods: a) light-off curves and b) CO_2 yield as a function of the reaction temperature.

Figure 5. iPrOH catalytic oxidation over the Mn_2O_3 catalysts synthetized by different preparation methods in the present study: a) light-off curves, b) acetone and c) CO_2 yields as a function of the reaction temperature, after three catalytic cycles.

Figure 6. Comparison between single and binary VOCs mixture oxidation over the Mn_2O_3 catalysts synthetized by different preparation methods: a) toluene and b) iPrOH conversions *vs.* reaction temperature and c) acetone and d) CO_2 yields after three catalytic cycles. Note that to simplify the tendency, only the CO_2 yields observed under a binary mixture are presented in this figure 6d.

Figure 7. *In-situ* DRIFTS spectra of the toluene catalytic oxidation over CG-1 catalyst.

Figure 8. *In-situ* DRIFTS of toluene under oxygen-free conditions over the CG-1 catalyst.

Figure 9. *In-situ* DRIFTS spectra of the iPrOH catalytic reaction over CG-1 catalyst.

Figure 10. In situ DRIFTS spectra of the iPrOH under oxygen-free conditions over CG-1 catalyst.

Figure 11. *In-situ* DRIFTS spectra recorded from the mixture catalytic oxidation of toluene and iPrOH over CG-1 catalyst under oxygen conditions.

Figure 12. *In-situ* DRIFTS spectra recorded at 35 ºC for single toluene or single iPrOH (first step of the sequential adsorption), as well as after simultaneous VOCs introduction and after sequential adsorption of iPrOH or toluene on preliminarily VOC-adsorbed surface (at 35 ºC) over CG-1 catalyst.

Figure 13. *In-situ* DRIFTS spectra recorded at 200 ºC for single toluene, single iPrOH and VOCs mixture, as well as after sequential introduction of iPrOH or toluene on preliminarily VOC-adsorbed surface (at 35 ºC) over CG-1 catalyst.

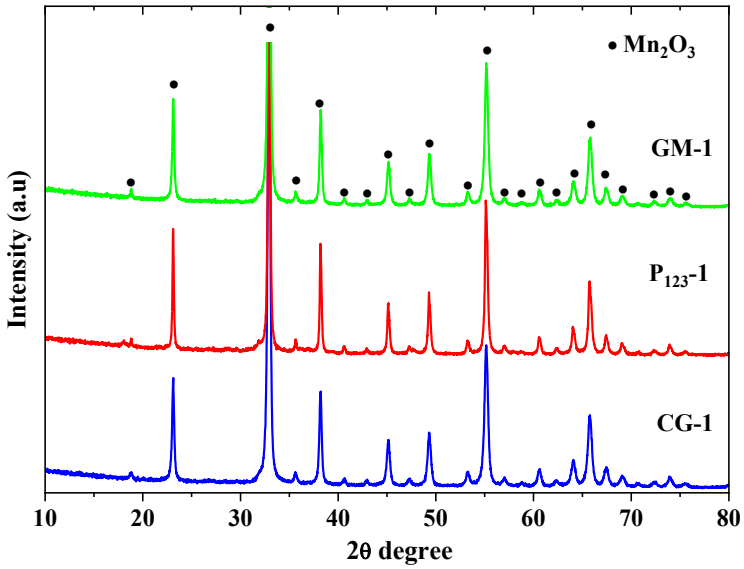

Figure 1. XRD diffractograms of the synthetized Mn_2O_3 catalysts by Citrate-Gel (CG-1), P_{123} surfactant (P_{123}-1) and Glycerol precipitation (GM-1) preparation methods.

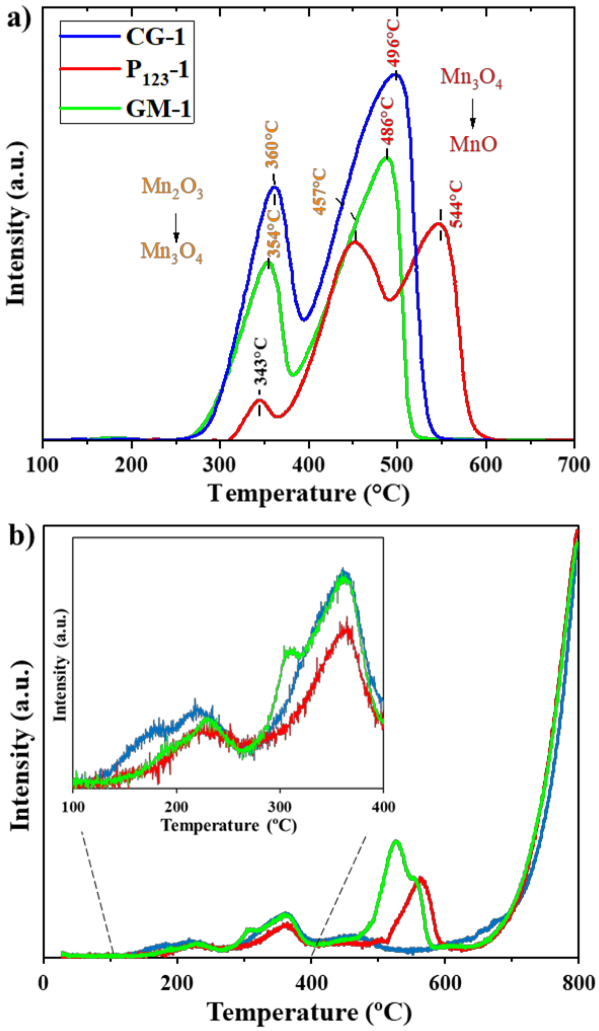

Figure 2. a) H_2-TPR and b) O_2-TPD profiles of Mn_2O_3 catalysts prepared by Citrate-Gel, P_{123} surfactant and glycerol precipitation methods. The inset of Figure 2b shows the oxygen desorption in the temperature range corresponding with physisorbed and chemisorbed oxygen species.

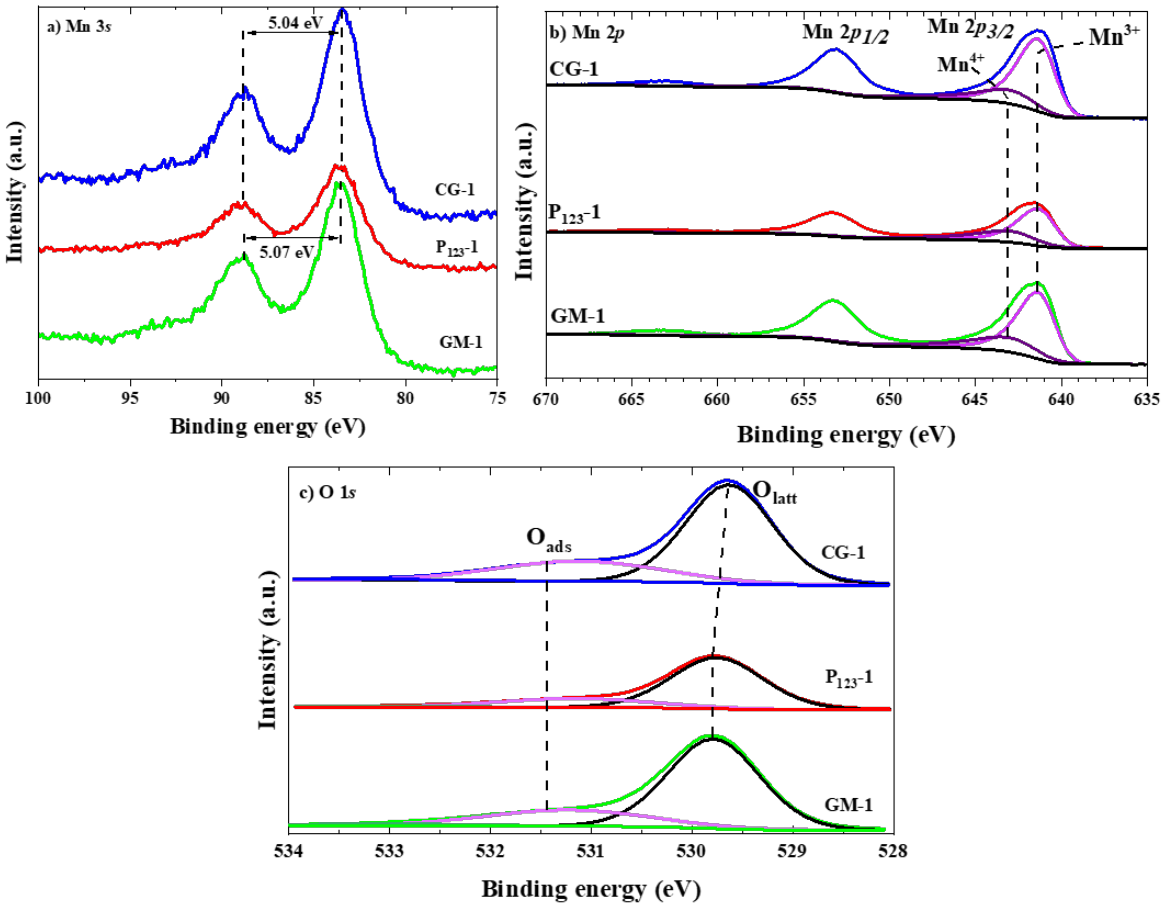

Figure 3. High-resolution XPS results for Mn_2O_3 catalysts; a) Mn 3*s*, b) Mn 2*p* and c) O 1*s*.

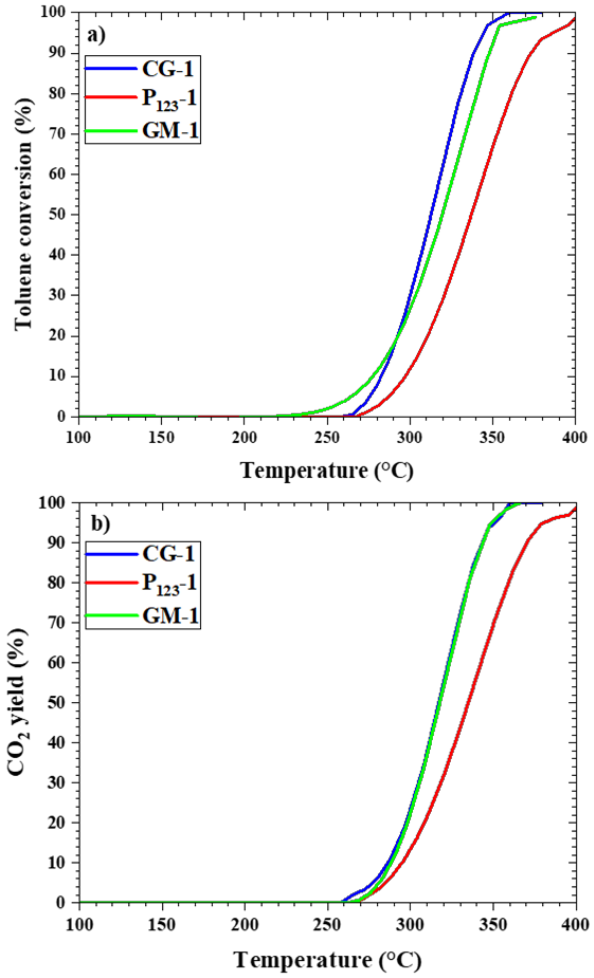

Figure 4. Single toluene catalytic oxidation over the Mn_2O_3 catalysts synthetized by different preparation methods: a) light-off curves and b) CO_2 yield as a function of the reaction temperature.

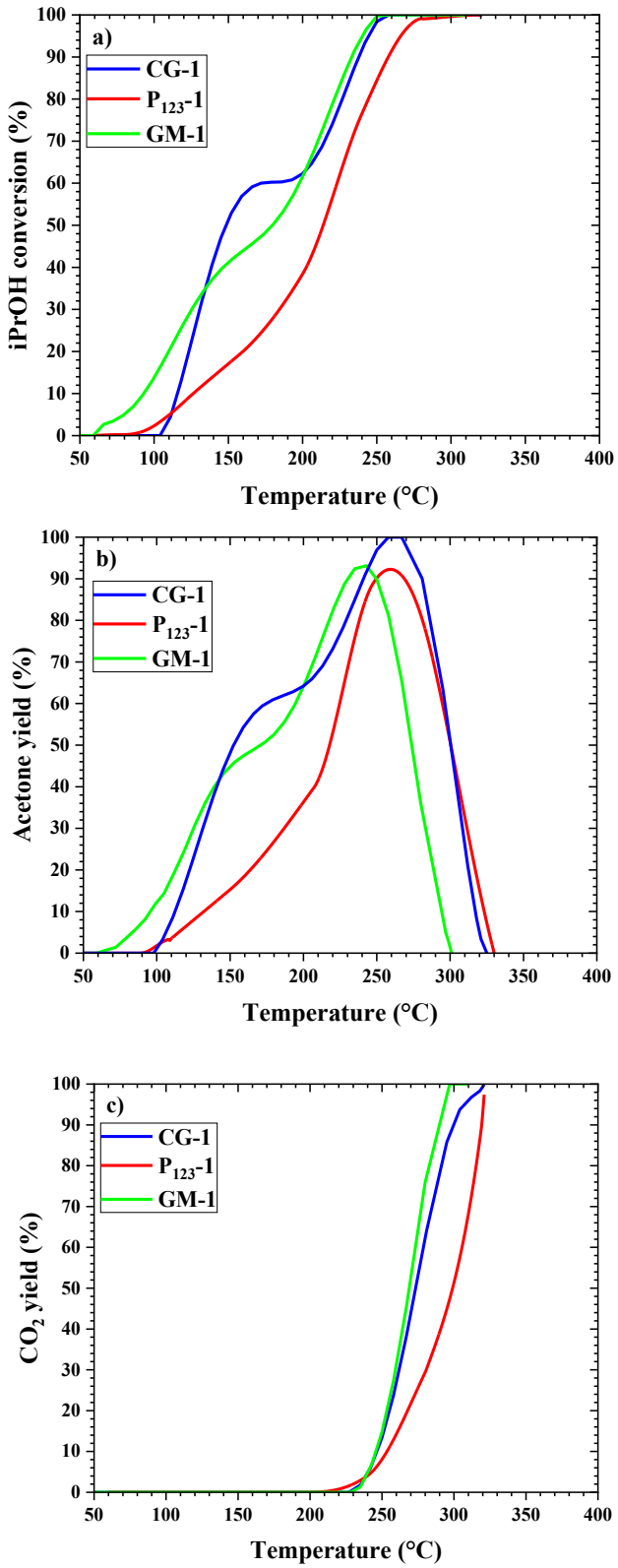

Figure 5. iPrOH catalytic oxidation over the Mn_2O_3 catalysts synthetized by different preparation methods in the present study: a) light-off curves, b) acetone and c) CO_2 yields as a function of the reaction temperature, after three catalytic cycles.

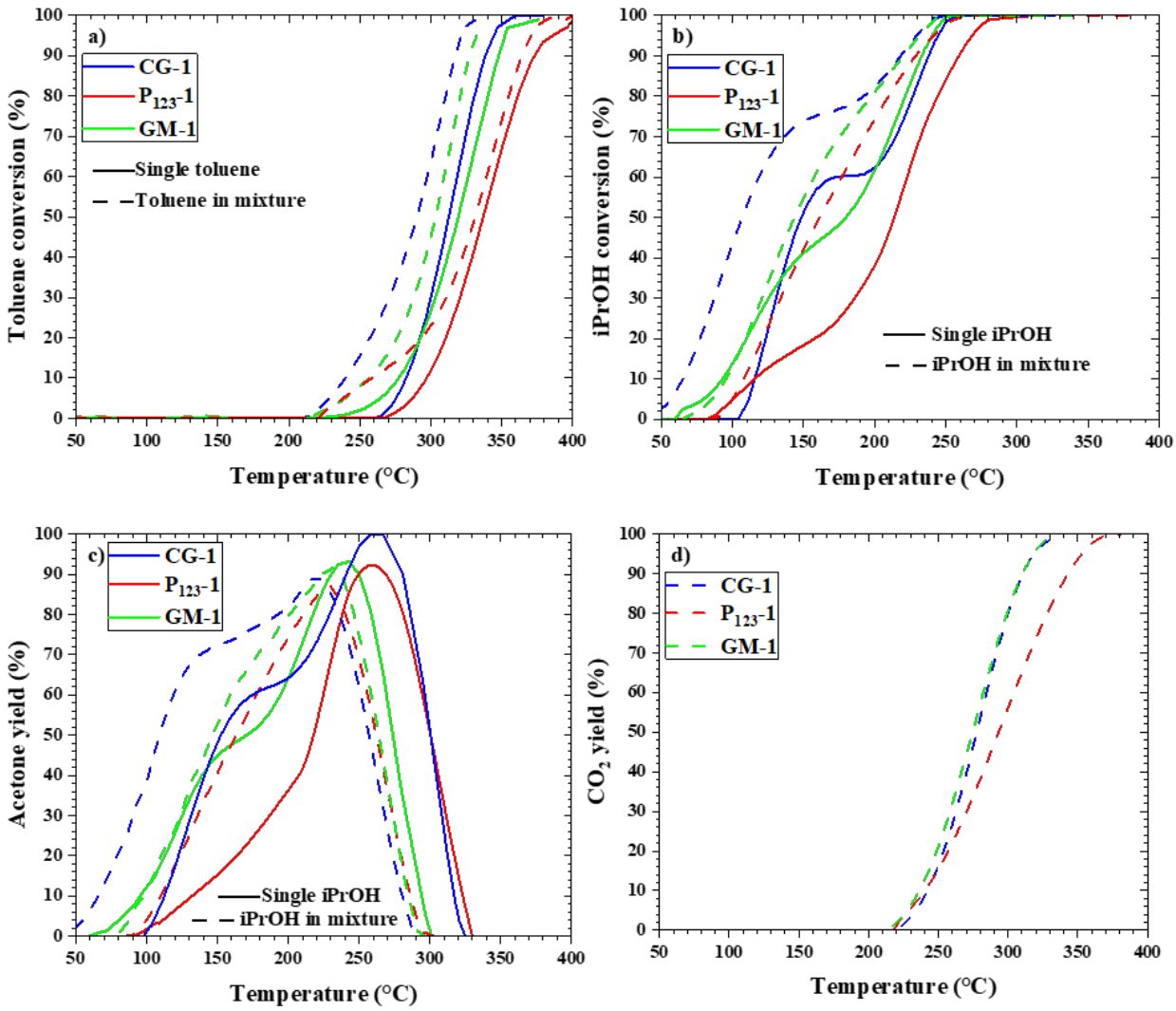

Figure 6. Comparison between single and binary VOCs mixture oxidation over the Mn_2O_3 catalysts synthetized by different preparation methods: a) toluene and b) iPrOH conversions *vs.* reaction temperature and c) acetone and d) CO_2 yields after three catalytic cycles. Note that to simplify the tendency, only the CO_2 yields observed under a binary mixture are presented in this figure 6d.

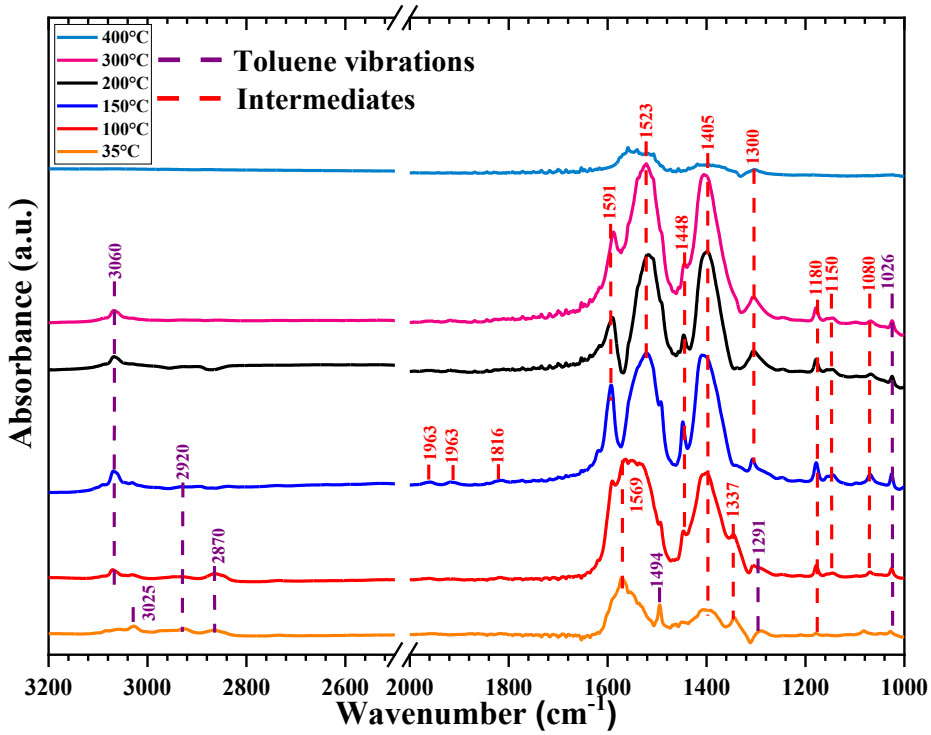

Figure 7. *In-situ* DRIFTS spectra of the toluene catalytic oxidation over CG-1 catalyst.

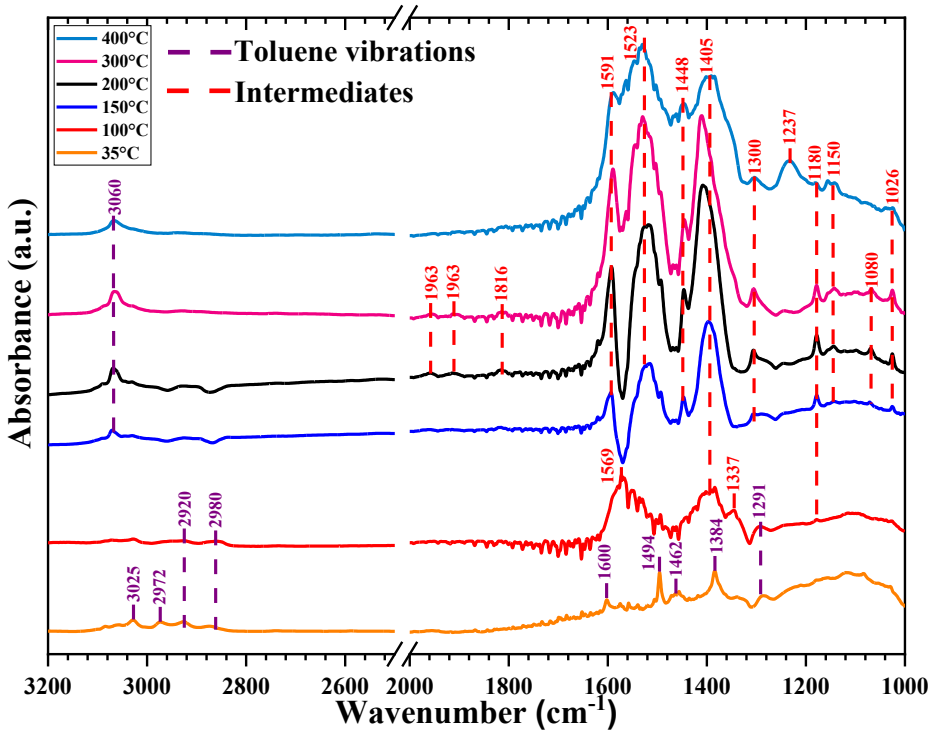

Figure 8. *In-situ* DRIFTS of toluene under oxygen-free conditions over the CG-1 catalyst.

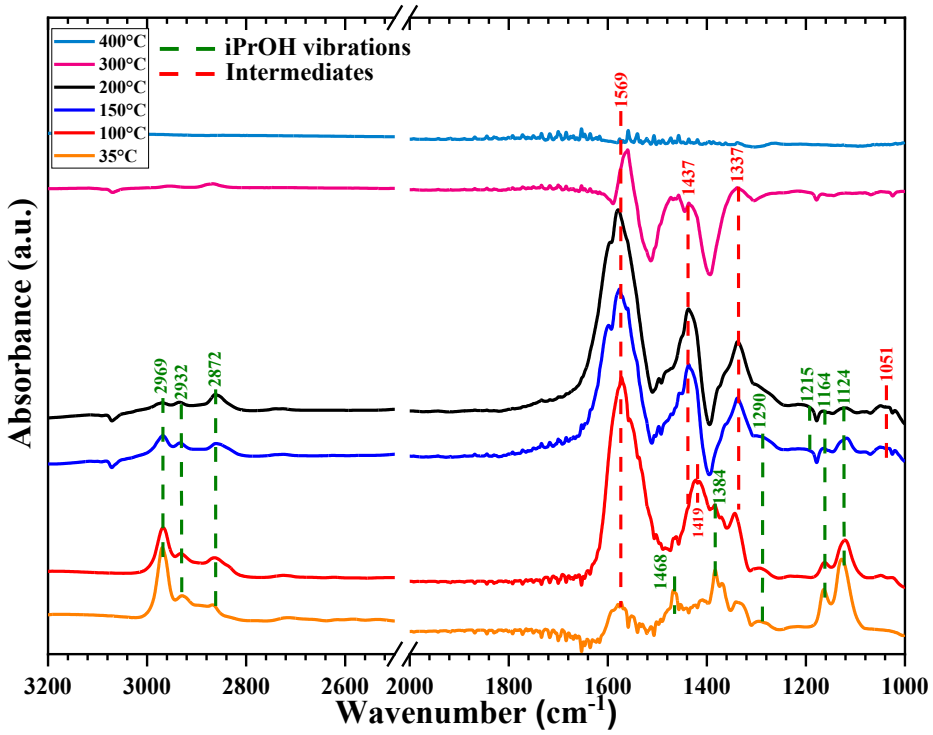

Figure 9. *In-situ* DRIFTS spectra of the iPrOH catalytic reaction over CG-1 catalyst.

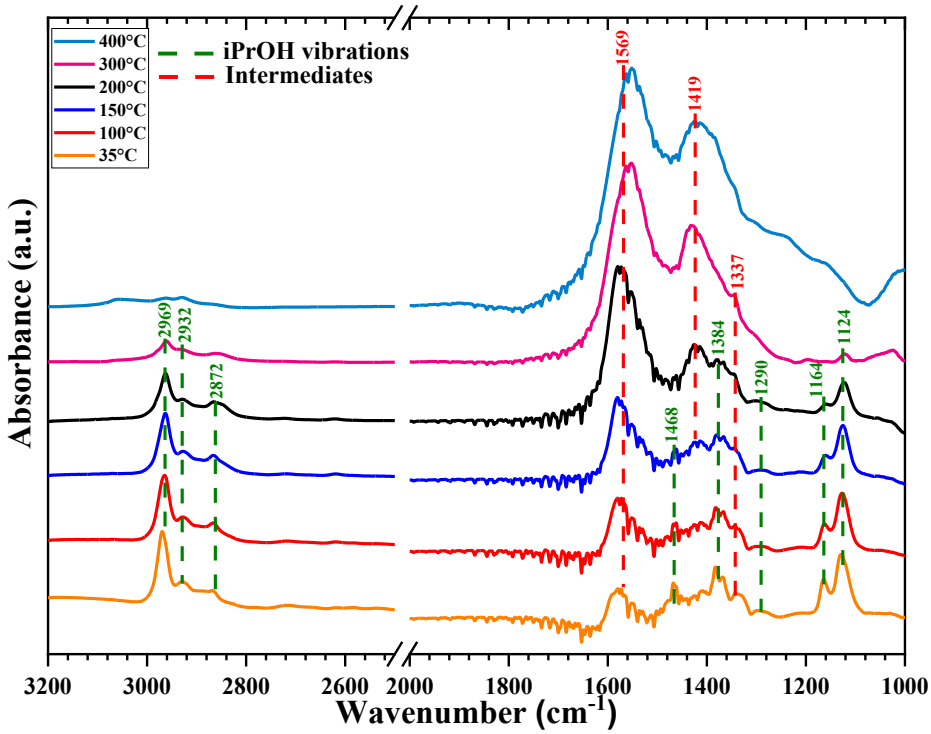

Figure 10. In situ DRIFTS spectra of the iPrOH under oxygen-free conditions over CG-1 catalyst.

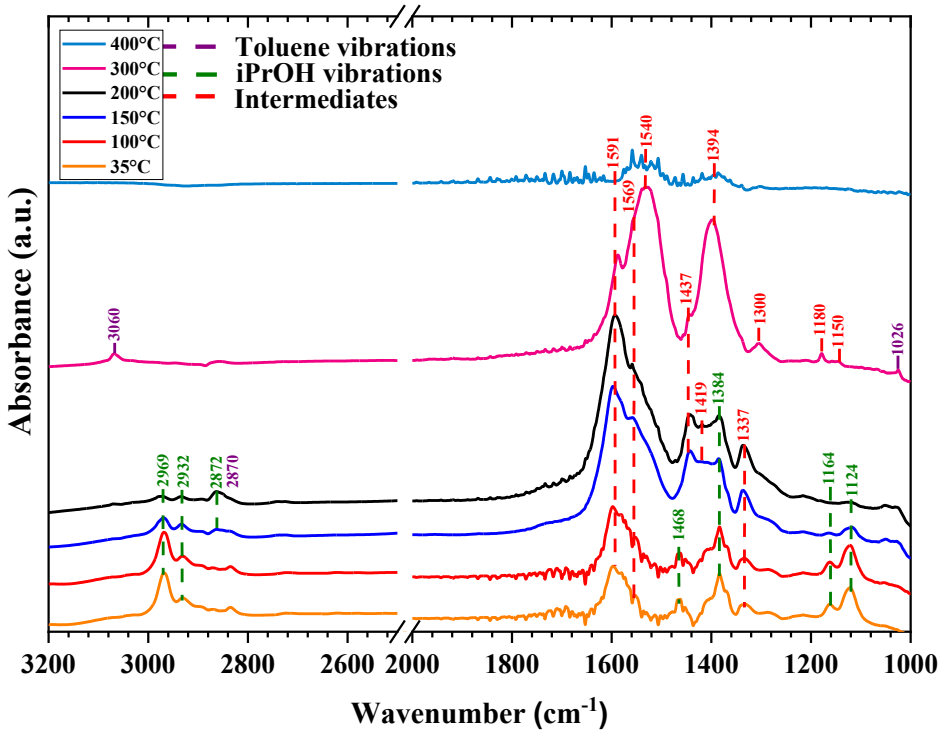

Figure 11. *In-situ* DRIFTS spectra recorded from the mixture catalytic oxidation of toluene and iPrOH over CG-1 catalyst under oxygen conditions.

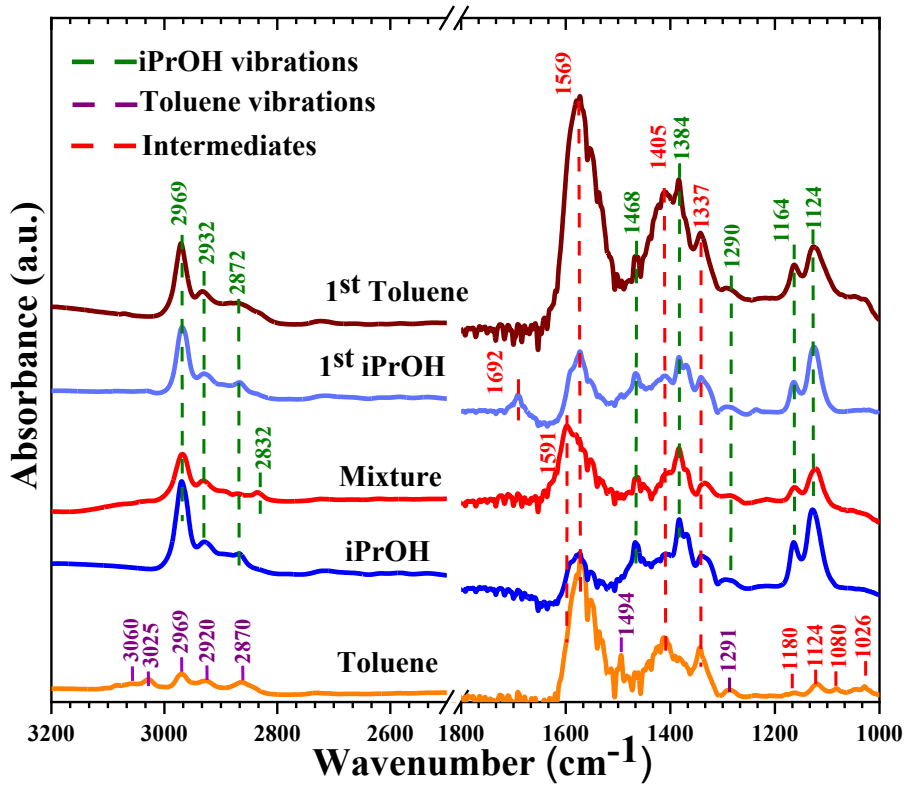

Figure 12. *In-situ* DRIFTS spectra recorded at 35 ºC for single toluene or single iPrOH (first step of the sequential adsorption), as well as after simultaneous VOCs introduction and after sequential adsorption of iPrOH or toluene on preliminarily VOC-adsorbed surface (at 35 ºC) over CG-1 catalyst.

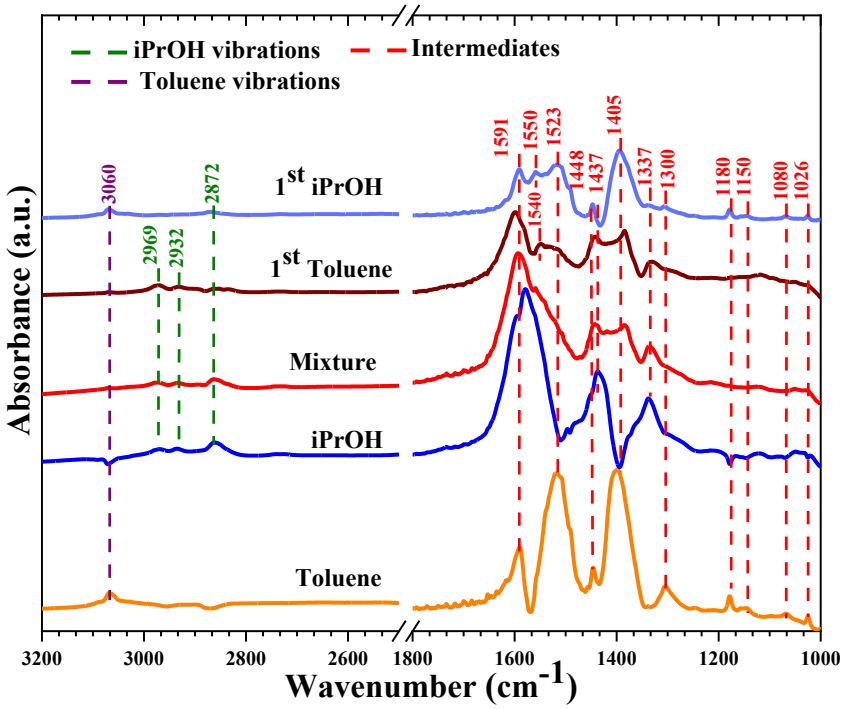

Figure 13. *In-situ* DRIFTS spectra recorded at 200 ºC for single toluene, single iPrOH and VOCs mixture, as well as after sequential introduction of iPrOH or toluene on preliminarily VOC-adsorbed surface (at 35 ºC) over CG-1 catalyst.

Revised Graphical Abstract

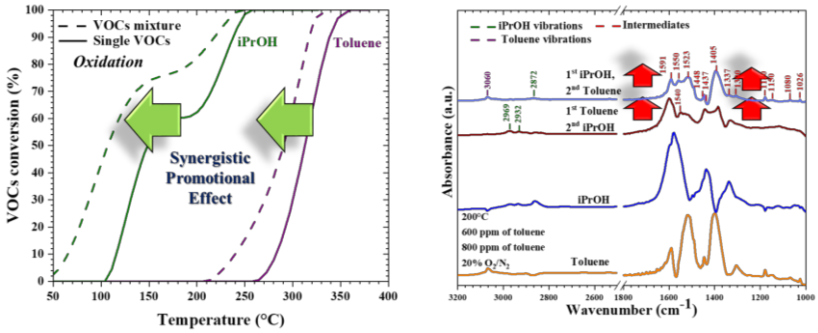

Highlights

- Mn_2O_3 oxides are active for the oxidation of toluene, 2-propanol and their mixture.
- Mn_2O_3 catalyst prepared by Citrate-Gel method has the best catalytic performances.
- The presence of both VOCs promoted the deep oxidation of each other on Mn_2O_3.
- The promotion effect of binary mixture above 200 ºC was proven by *in-situ* DRIFTS.
- DRIFTS allowed to identify the reaction intermediates in different scenarios.

Supplementary information

Toluene and 2-propanol mixture oxidation over Mn_2O_3 catalysts: Study of inhibition/promotion effects by in-situ DRIFTS

E.J. Moreno-Román, J. González-Cobos, N. Guilhaume, S. Gil*

Univ Lyon, Université Lyon 1, CNRS, UMR 5256, IRCELYON, 2 avenue Albert Einstein, Villeurbanne, F-69622, France.

Corresponding author: *sonia.gil@ircelyon.univ-lyon1.fr

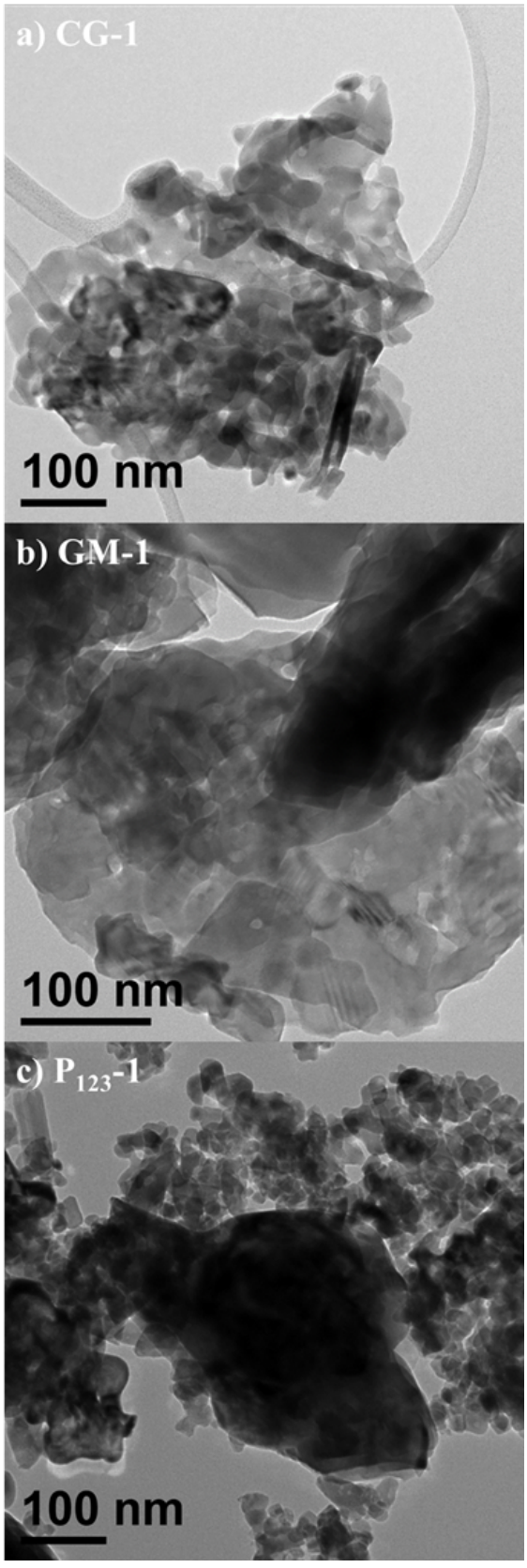

Figure S1. TEM images of Mn_2O_3 catalysts synthetized by (a) Citrate-Gel (CG-1), (b) Glycerol precipitation (GM-1) and (c) P_{123} surfactant (P_{123}-1).

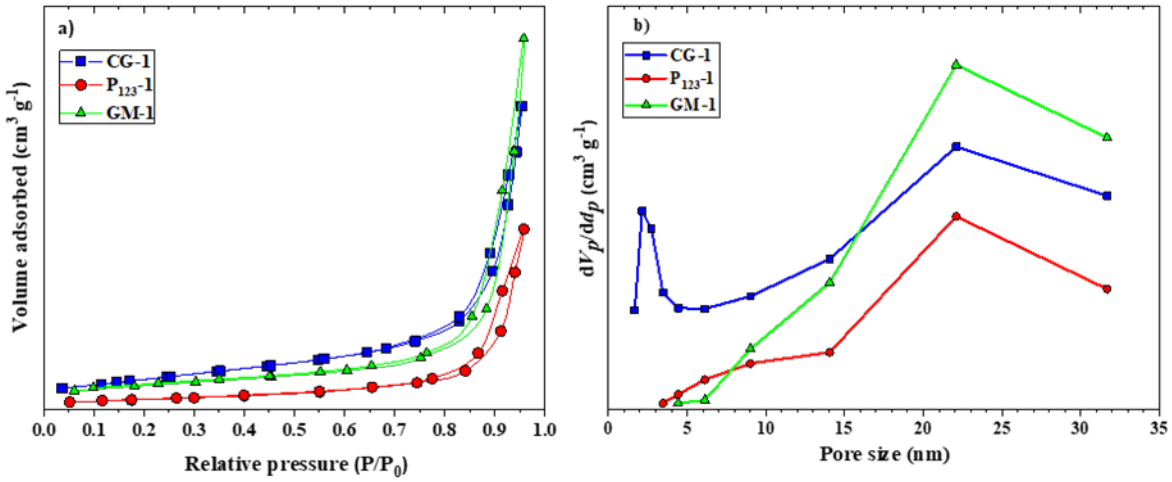

Figure S2. a) N_2 adsorption-desorption isotherms and b) pore size distribution of the Mn_2O_3 catalysts synthetized by different methods.

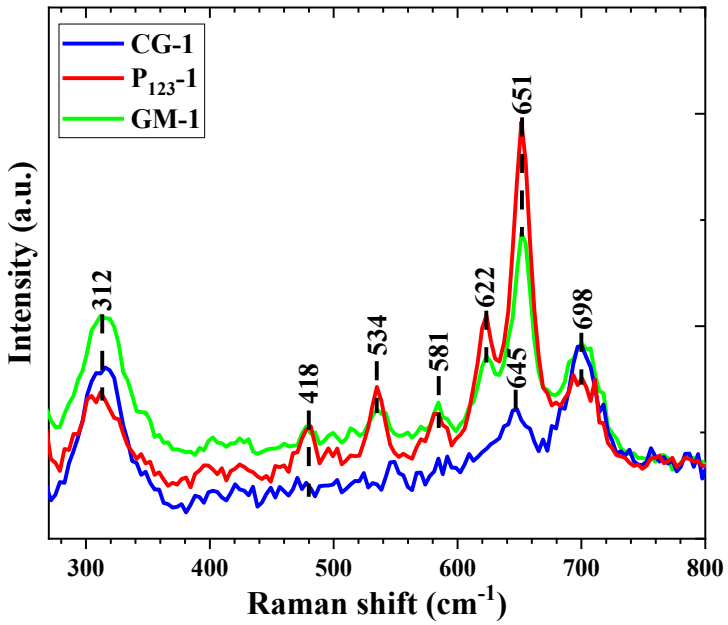

Figure S3. Raman spectra over Mn_2O_3 catalysts synthetized by different preparation methods.

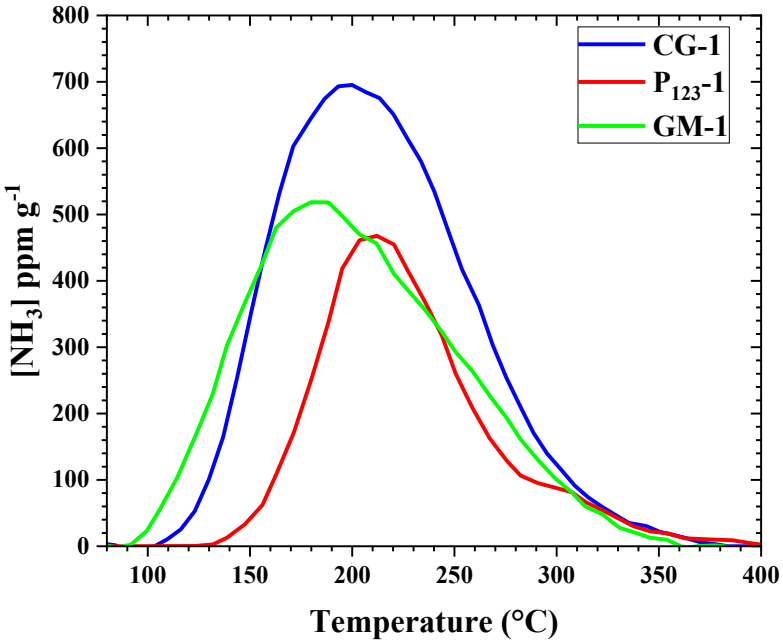

Figure S4. NH_3-TPD profiles over the Mn_2O_3 catalysts synthetized by different preparation methods in the present study.

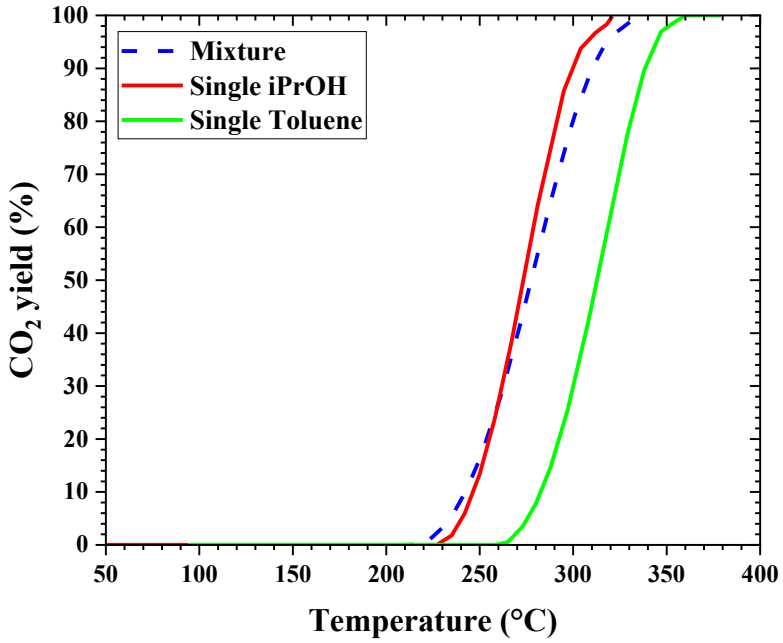

Figure S5. Comparison of CO_2 yields between single and binary VOCs mixture oxidation over CG-1 catalyst after three catalytic cycles.

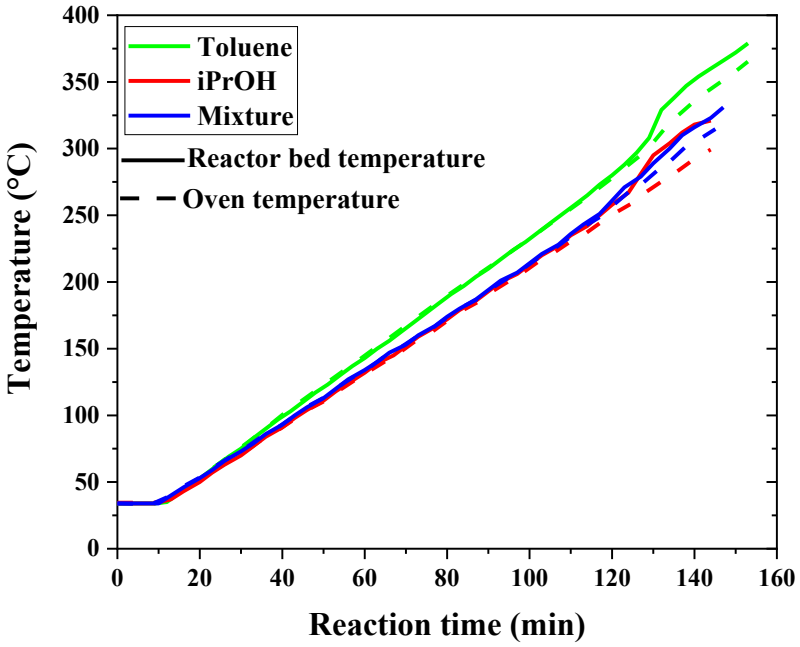

Figure S6. Variation of the temperature registered inside the reactor with respect to that controlled at the furnace due to the exothermic effect taking place during the light-off tests performed on catalyst CG-1 in single and binary VOCs oxidation.

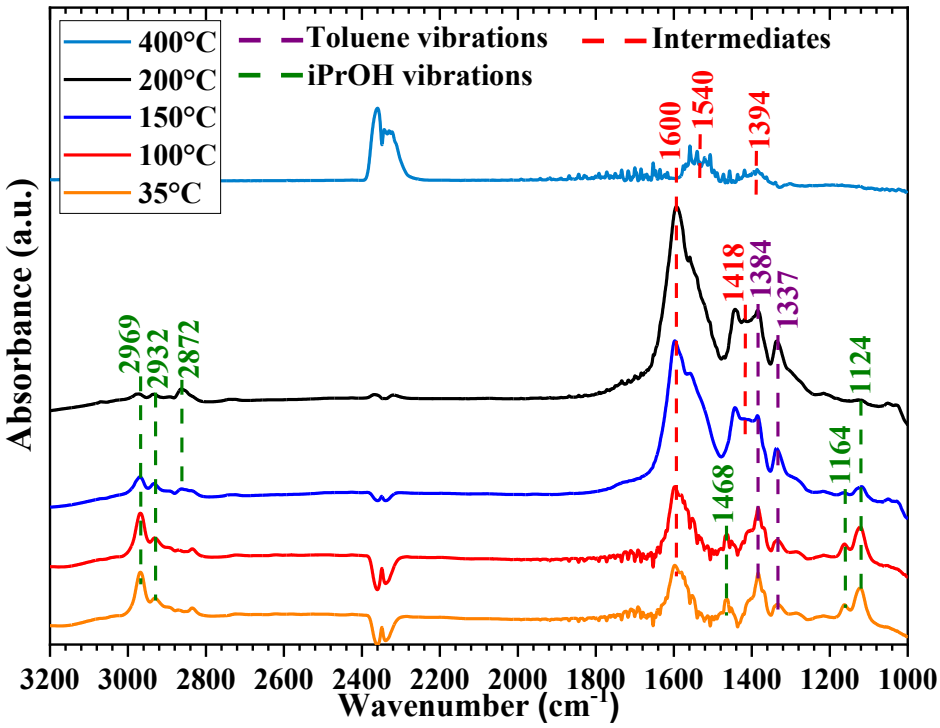

Figure S7. *In-situ* DRIFTS spectra (full wavenumber range) recorded from the mixture catalytic oxidation of toluene and iPrOH over CG-1 catalyst.